Seasonal Patterns of Vegetated Areas and Its Impact on Urban Heat Island, A Case Study of Xi'an, China

XUANMAN BAI
Enschede, The Netherlands, February, 2015

SUPERVISORS:
Drs, J. M. Looijen
Dr. Tiejun. Wang

Seasonal Patterns of Vegetated Areas and Its Impact on Urban Heat Island, A Case Study of Xi'an, China

XUANMAN BAI
Enschede, The Netherlands, February, 2015

Thesis submitted to the Faculty of Geo-Information Science and Earth Observation of the University of Twente in partial fulfilment of the requirements for the degree of Master of Science in Geo-information Science and Earth Observation.
Specialization: Geographic Information for Natural Resources and Environmental Management

SUPERVISORS:
Drs, J. M. Looijen
Dr. Tiejun. Wang

THESIS ASSESSMENT BOARD:
Dr. Ir. C.A.J.M. de Bie (Chair)
Prof. Dr. Ing. W. Verhoef (External Examiner, Department of Water Resources, ITC, University of Twente)

ABSTRACT

The urban heat island (UHI) refers to the phenomenon of higher atmospheric and surface temperature which happens in urban areas than in the surrounding rural areas. The previous researches mainly focused on analyze the green space in urban areas to mitigate the urban heat islands effect. However, little is researched to discuss the effect of rural areas on urban heat islands. The objective of this research is to investigate the effects of seasonal changes of the green-vegetated areas on the urban heat island in Xi'an city and its surrounding regions.

In the study, the green-vegetated areas in four seasons were mapped through land cover maps using Maximum Likelihood method based on the Landsat 8 data. The land surface temperatures in four seasons were calculated by Split-Window (SW) algorithm using Landsat 8 thermal bands 10 and 11. The spatial patterns of green vegetated areas and land surface temperature were quantified through five buffer zones. Consequently, the relationships between spatial patterns of green vegetation and land surface temperature were examined.

The results is that, in summer, the effect of green vegetations on the land surface temperature of built-up is clear negative within the areas away from city centre. However, in winter and spring, large proportion and areas of bare land may influence and counteract the cooling effect from green vegetation areas. the relationships between green vegetation and land surface temperature in built-up areas. The results from the relationship between the spatial patterns of green vegetation and urban heat islands show that the urban heat islands is a the combined effects from all land covers and especially the bare land which reflects higher land surface temperature.

ACKNOWLEDGEMENTS

0n the onset, I would like to express my deep sincere gratitude to my ITC supervisors Drs. J. M. Looijen and Dr. Tiejun. Wang for their continuous support and brilliant guidance through the learning process of this master thesis. Their guidance helped me throughout this research and in the writing of this thesis. Without their patience, motivation, enthusiasm, and immense knowledge, this work would not have been a success.

First and foremost, I appreciate the opportunity to study in the faculty of Geo-information Science and Earth Observation (ITC) of University of Twente, which opened my eyes to a broader vision. Most of my theoretical foundations were built in the Department of Natural Resources. I am very grateful that I could have this chance to touch the new course and learn what I am interested.

During the my period of 14 months in ITC, many friends helped to colour my life. I thank all my NRM classmates who assisted me a lot in my courses and during the research period. At the same time, I would like to extend my thanks to all of the people who supported me during the research in ITC as an MSc student.

Furthermore, I would like to thank all my friends in China. They encouraged and offered continuous support when I need courage and reassurance to keep going on. I know they are waiting for me. Thanks my friends, you all are my precious treasures.

Last but not least, my greatest appreciation goes to my family: my parents Runlin Bai and Yanping Hao, for giving birth to me, giving eternal love to me and supporting me spiritually throughout my life. Daddy and Mommy, I love you so much. Thank you very very much.

TABLE OF CONTENTS

1. Introduction.....1
   1.1. Background.....1
   1.2. Research justification.....2
   1.3. Research objectives and questions.....2
   1.4. Research hypothesis.....3
   1.5. Structure of the thesis.....3
2. Study area and materials.....5
   2.1. Study area.....5
   2.2. Landsat 8 images.....6
3. Methods.....9
   3.1. Atmospheric correction of Landsat 8 images.....9
   3.1. Land cover classification and accuracy assessment.....12
   3.2. Calculating land surface temperature from Landsat 8 images.....14
   3.3. Statistical analysis.....19
4. Results.....21
   4.1. Spatial patterns of green-vegetated areas in four seasons.....21
   4.2. Spatial patterns of land surface temperature in four seasons.....27
   4.3. Relationship analysis between green-vegetated areas and urban heat island.....33
5. Discussions.....37
   5.1. Quantification for spatial patterns of green-vegetated areas in four seasons.....37
   5.2. Quantification for the spatial patterns of land surface temperature in four seasons.....37
   5.3. The relationship between green-vegetated areas and urban heat island.....38
6. Conclusions and recommendations.....39
   6.1. General conclusion.....39
   6.2. Recommendations.....39

List of references.....41

Appendix 1.....45

Appendix 2.....48

LIST OF FIGURES

Figure 1: Framework of the research approaches. 4
Figure 2: Landsat 8 image of the study area Xi'an City, China in summer. (R, G, B: 4, 3, 2). 5
Figure 3: Bandpass wavelength for Landsat 8 OLI and TIRS sensors, compared to Landsat 7 ETM+ sensor. 7
Figure 4: Comparison of NDVI maps before and after atmospheric correction, dated 29th September 2013 11
Figure 5: Band combination applied, dated 25th June, 2013 (R,G,B: 5,6,2,) 13
Figure 6: NDVI map for Landsat 8 data, dated 25th June, 2013. 13
Figure 7: High resolution aerial image of the study area, data from Google Earth. 13
Figure 8: Five buffer zones drawn in the study area. 14
Figure 9: Land cover classification maps: (a) summer; (b) autumn; (c) winter; (d) spring. 22
Figure 10: Area proportion of green vegetation in each buffer zone, four seasons. 26
Figure 11: Area proportion of bare land in each buffer zone, four seasons. 26
Figure 12: Normalized land surface temperature in summer (a), autumn (b), winter (c) and spring (d). 27
Figure 13：Land surface temperature maps (in Kelvin)：(a) summer; (b) autumn; (c) winter; (d) spring 29
Figure 14: The error bar for the land surface temperature of sample points in built-up areas in summer 31
Figure 15: The error bar for the land surface temperature of sample points in built-up areas in autumn 31
Figure 16: The error bar for the land surface temperature of sample points in built-up areas in winter 31
Figure 17: The error bar for the land surface temperature of sample points in built-up areas in spring 31
Figure 18: The error bar for the land surface temperature of sample points in each buffer in summer. 33
Figure 19: The error bar for the land surface temperature of sample points in each buffer in autumn. 33
Figure 20: The error bar for the land surface temperature of sample points in each buffer in winter. 33
Figure 21: The error bar for the land surface temperature of sample points in each buffer in spring. 33
Figure 22: Four box-plots for the land surface temperature in built-up areas: (a) summer; (b) autumn; (c) winter; (d) spring. 35
Figure 23: Four box-plots for the land surface temperature: (a) summer; (b) autumn; (c) winter; (d) spring 36
Figure 24: Brightness temperature maps for bands 10 (left) and 11 (right) in the image of summer (in Kelvin). 45
Figure 25: Brightness temperature maps for bands 10 (left) and 11 (right) in the image of autumn (in Kelvin). 46
Figure 26: Brightness temperature maps for bands 10 (left) and 11 (right) in the image of winter (in Kelvin) 46
Figure 27: Brightness temperature maps for bands 10 (left) and 11 (right) in the image of spring (in Kelvin). 47

Figure 28: Land surface emissivity of band 10 for four images: (a) summer; (b) autumn; (c) winter; (d) spring. 49

LIST OF TABLES

Table 1: Specific objectives and research questions. 2
Table 2: Spectral characteristics of Landsat 8. 7
Table 3: Input parameters in the ATCOR 2 module 10
Table 4: The c_0 and c_1 coefficients of bands 1-7 for Landsat 8 image of June 25, 2013. 10
Table 5: The range of NDVI values before and after atmospheric correction for four seasons. 11
Table 6: Comparisons between NDVI values for four land cover type before and after atmospheric correction in four seasons 12
Table 7: The number of sample points of land cover types in four seasons. 13
Table 8: Landsat 8 reflectance rescaling coefficients for band 10 and band 11 15
Table 9: Landsat 8 thermal constants for band 10 and band 11. 16
Table 10: Emissivity values for different typical land feature in Landsat 8. 17
Table 11: Coefficients for the Split-Window Split-Window (SW) algorithm 19
Table 12: The number of sample points in built-up areas , in each buffer zone for the four seasons. 20
Table 13: Confusion matrix for accuracy assessment in four season images. 23
Table 14: Accuracy assessment of classified Landsat 8 images for four seasons 24
Table 15: The result of Z-test for Kappas. 24
Table 16: Area proportion of green vegetation and bare land in five buffer zone, four seasons. 24
Table 17: Mean and Std. Deviation of the land surface temperature of sample points in built-up areas in summer 30
Table 18: Mean and Std. Deviation of the land surface temperature of sample points in built-up areas in autumn. 30
Table 19: Mean and Std. Deviation of the land surface temperature of sample points in built-up areas in winter. 30
Table 20: Mean and Std. Deviation of the land surface temperature of sample points in built-up areas in spring. 30
Table 21: Mean and Std. Deviation of the land surface temperature of sample points in each buffer in summer. 32
Table 22: Mean and Std. Deviation of the land surface temperature of sample points in each buffer in autumn. 32
Table 23: Mean and Std. Deviation of the land surface temperature of sample points in each buffer in winter. 32
Table 24: Mean and Std. Deviation of the land surface temperature of sample points in each buffer in spring 32
Table 25: The result of Z-test for proportions, in summer 34
Table 26: The result of Z-test for proportions, in autumn. 34
Table 27: The result of Z-test for proportions, in winter. 34
Table 28: The result of Z-test for proportions, in spring. 34
Table 29: Land surface emissivity of bands 10 and 11 for each land cover type. 49

1. INTRODUCTION

1.1. Background

It is well known that global warming is an indisputable fact. According to IPCC (2007), 1998 and 2005 were the warmest two years in the instrumental global surface air temperature record since 1850. Also, the global average surface temperature has increased, especially since about 1950. The 100-year trend (1906–2005) of 0.74°C ± 0.18°C is larger than the 100-year warming trend at the time of 1901–2000 of 0.6°C ± 0.2°C due to additional warm years. The total temperature increase from 1850-1899 to 2001-2005 is 0.76°C ± 0.19°C. The rate of warming averaged over the last 50 years (0.13°C ± 0.03°C per decade) is nearly twice that for the last 100 years. Population growth and urbanization are the main drivers for global temperature rise. It is reported that more than half of the world's population now live in urban area and the urban population is predicted to reach 81% by 2030 (UNFPA, 2008).

Due to rapid urbanization, it appears a phenomenon that higher atmospheric and land surface temperatures occur in urban areas than in the surrounding rural areas (Maimaitiyiming et al., 2014). This observation, called urban heat island (UHI), was first described by Luke Howard (1833) in the early of 19th century. Rapid urbanization causes a decrease in green-vegetated areas and an increase of the built-up surface (Buyadi et al., 2013). The land surface is modified into built surface which can store the short-wave radiation effectively (Maimaitiyiming et al., 2014). This urban structure can trap incoming solar radiation during the day and then at night, slowly dissipate (Gago et al., 2013). Therefore, the land surface temperature (LST) raised and it is crucial to the themes on urban climatology, global environmental change and human-environmental interactions (Siti Nor Afzan Buyadi et al., 2013).

Many researchers tried to investigate the driving forces leading to the increasing temperature gap between urban and rural areas and explore the way to mitigate urban heat island effects. Their studies were always analyzed using two methods (Liu et al., 2006). One way to study the UHI effect is using LST derived from remote sensing technique. Imhoff et al. (2010) used LST from MODIS in a spatial analysis to assess the urban heat island surface temperature distribution. Other remote sensing information, such as Normalized Difference Vegetation Index (NDVI), is used as indicator to estimate the relationship between LST and vegetation abundance. For example, Farina (2012) used NDVI to explore the interactions between LST and green-vegetation and her study showed that vegetation can provide for cooler microclimates through the process of evapotranspiration and increasing amounts of vegetation might prove to be a effective solution for mitigating UHI effect (Yuan & Bauer, 2007). However, the disadvantage of LST data is that it can be influenced by air conditions over time and cannot characterize the surface atmospheric temperature (Liu et al., 2006). It may only demonstrate the distribution of UHI qualitatively.

Another more traditional method to study UHI is using the surface air temperature data from meteorological stations. Many researchers paid attention to the changes of UHI within one day, one year and many years based on meteorological data (Zhang et al., 2010). Borbora and Das (2014) used half hourly temperature data measured at four fixed observation sites to analyze the daytime and night time UHI effect of summer in Guwahati, India. This kind of data can quantitatively describe the variation of UHI over a long period. However, it is hard to describe spatial distribution of UHI effect in accuracy (Liu et al., 2006) because of the discontinuous distribution of meteorological stations (Zhang et al., 2010). Still there is a high positive relationship between LST and surface air temperature (Schwarz et al., 2012)

1.2. Research justification

It has to be admitted that focusing on urbanization is an effective way to analyze UHI effect because urbanization negatively impacts the environment mainly by the production of pollution, the modification of the physical and chemical properties of the atmosphere, and the covering of the soil surface (Canada, 2009). However relatively little is done to address the effect of rural areas on UHI (Timothy et al., 2004). In rural areas surrounding urban areas, the vegetated areas occupy most of the land and those green areas contribute to the mitigation of UHI.

Temperatures in the vegetated area and it surroundings keep the temperature lower than within developed areas (Siti Nor Afzan Buyadi et al., 2013). Green spaces are particularly beneficial to improving the microclimate (B. Zhang et al., 2014). Zhang et al. (2010) analyzed the relationship between vegetation greenness and UHI effect in Beijing City of China and concluded that vegetation and temperature have a significant negative correlation, which means the higher the vegetation coverage is, the lower the temperature is. The reason is that vegetation usually has a higher evapotranspiration and lower emissivity than built-up areas (Weng, Lu, & Schubring, 2004). Evapotranspiration is a vital process that the water loss of a plant in the form of vapour released into the air and it produces the cooling of leaves and the air temperature around them (Gago et al., 2013). In addition to evapotranspiration, the shade from trees can also cool the atmosphere by interrupting solar radiation and thereby preventing the heating of air (Gago et al., 2013). Besides, as two major components of land use/ land cover (LU/LC) pattern, the composition of green space referring to the abundance and variety of land cover classes and the configuration of green spaces related to the spatial arrangements of land cover classes both have relationship with LST (Maimaitiyiming et al., 2014). The significant negative relationship between the vegetation composition and LST has been well documented, however, the relationship between spatial characteristics and configuration of vegetation patches and LST is less studied (Li et al., 2012; Maimaitiyiming et al., 2014).

Apart from spatial arrangement of rural green-vegetated areas, Yuan and Bauer (2007) estimated the LST from four different seasons for the Twin Cities, Minnesota, and concluded that the relationship between LST and NDVI is changing with the changes in seasons. Moreover, the land cover changes in urban areas within one year can be assumed as stable. Therefore the spatial patterns of green-vegetated areas with the seasonal changes derived from the phenology characteristics will be discussed in this study.

1.3. Research objectives and questions

1.3.1. Overall objective

To investigate the effects of seasonal changes of the green-vegetated areas on the urban heat island in Xi'an city and its surrounding regions.

1.3.2. Specific objectives and research questions

Table 1: Specific objectives and research questions.

No.	Specific objectives	Research questions
1	To quantify spatial and temporal patterns of green-vegetated areas in and around Xi'an City;	What are the seasonal distribution patterns of the green-vegetated areas in and around Xi'an City?
2	To estimate and explore spatial and temporal patterns of land surface temperature in and around Xi'an City;	What is the seasonal pattern of the land surface temperature in and around Xi'an City?
3	To examine the relations between the seasonal vegetated green spaces in and around the city and urban heat distribution.	Does the seasonal patterns of green-vegetated areas in and around the city areas have a significant effect on urban heat island?

1.4. Research hypothesis

Null Hypothesis: The seasonal and spatial pattern of rural green-vegetated areas has no significant effect on urban heat island distribution.

Alternatives Hypothesis: The seasonal and spatial pattern of rural green-vegetated areas has a significant effect on urban heat island distribution.

1.5. Structure of the thesis

The present research is elaborated in five chapters: Introduction, Study area and materials used, Methodology, Results and discussion, and Conclusions and recommendations.

Chapter 1. Introduction

This chapter deals with the introduction, motivation behind this research, research objectives, research questions and hypothesis.

Chapter 2. Study area and materials used

In this chapter, the information of study area which includes geographical location and climate is given, and data/materials used are contained.

Chapter 3. Methodology

This chapter describes methods for data processing, image classification, estimation of emissivity and land surface temperature and data analysis.

Chapter 4. Results

The output of each step is available in form of graphs and tables. The results about land cover classification, estimation of land surface temperature and statistic analysis are presented.

Chapter 5. Discussion

In this chapter, the results obtained in the previous chapter are discussed to answer the predefined research questions.

Chapter 6. Conclusions and recommendations

In this last chapter, the conclusions and recommendations for future research are formulated.

Figure 1 shows the overall framework of the research.

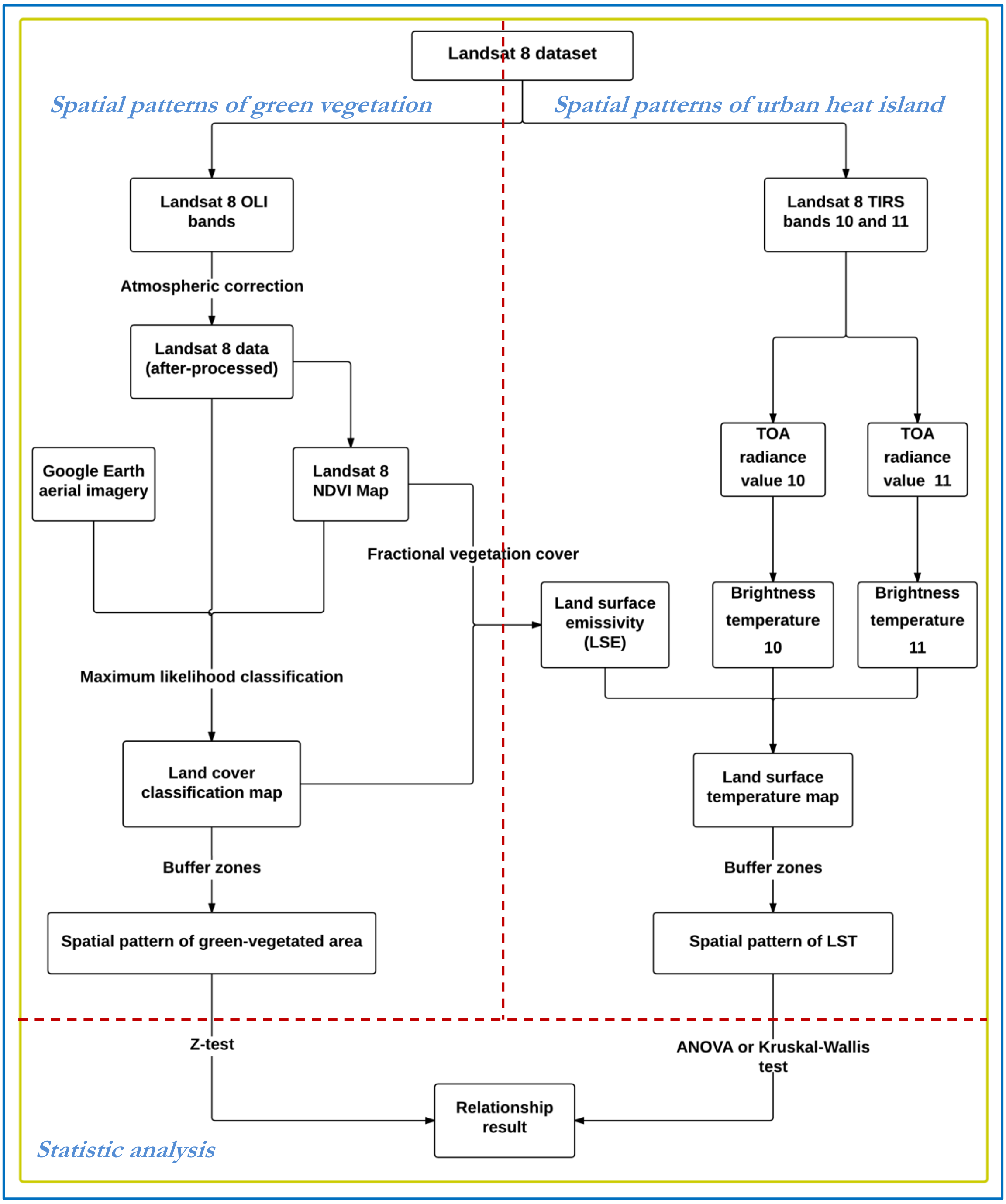

Figure 1: Framework of the research approaches.

2. STUDY AREA AND MATERIALS

2.1. Study area

Xi'an, the city and capital of Shaanxi province, north-central China, is one of the Four Great Ancient Capitals of China, having held the position under several of the most important dynasties in Chinese history. Xi'an metropolitan area consists 13 districts with approximately 8.6 million permanent residents in an area of approximately 9983 km2 (Xi'an Municipal Statistics Bureau, 2013).

Xi'an city is situated 33°39'–34°45' N and 107°40'–109°49' E, about 410 m above sea level. The city site is on a low plain on the south bank of the Wei River. Just to the south the Qin (Tsingling) Mountains rise dramatically above the plain. The study area (Figure 1) is a circle, extending 20 km from city centre (The Bell Tower) to the east, west, north and south directions.

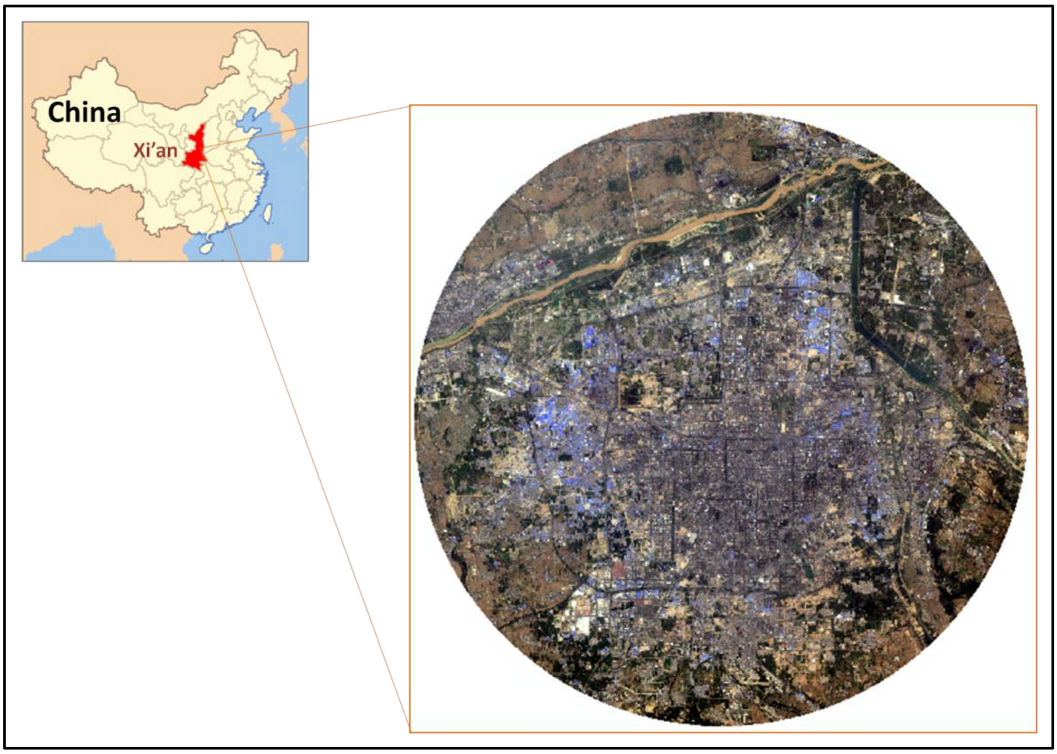

Figure 2: Landsat 8 image of the study area Xi'an City, China in summer. (R, G, B: 4, 3, 2).

Xi'an has a temperate climate that is influenced by the East Asian monsoon, classified under the Köppen climate classification as situated on the borderline between a semi-arid climate (BSk) and humid subtropical climate (Cwa). Xi'an has a continental climate with hot summers and cold dry winters. Spring, summer, autumn and winter are from March to May, June to August, September to November and December to February, respectively. The rainy season begins in May and continues to September which can receive over 80% of the annual precipitation. Snow occasionally falls in winter but rarely settles for long. Dust storms often occur during March and

April as the city rapidly warms up. Summer months also experience frequent but short thunderstorms. The annual prevailing wind of Xi'an mainly comes from the NE.

2.2. Landsat 8 images

Landsat 8 dataset is used in this research. The data is used for the preparation of land cover maps and estimation of the land surface temperature (LST).

Landsat 8 is an American Earth observation satellite launched on February 11, 2013. It is the eighth satellite in the Landsat program; the seventh to reach orbit successfully. Formerly called the Landsat Data Continuity Mission (LDCM), it is a collaboration between NASA and the United States Geological Survey (USGS).

Landsat 8 carries two instruments: The Operational Land Imager (OLI) sensor includes refined heritage bands, along with three new bands: a deep blue band for coastal/aerosol studies, a shortwave infrared band for cirrus detection, and a Quality Assessment band. The Thermal Infrared Sensor (TIRS) sensor provides two thermal bands. These two sensors provide seasonal coverage of the global landmass at a spatial resolution of 30 meters (visible, NIR, SWIR); 100 meters (thermal); and 15 meters (panchromatic) (Table 1). Improved signal to noise performance enable better characterization of land cover state and condition.

The spectral bands of the OLI sensor, while similar to Landsat 7's ETM+ sensor, provides enhancement from prior Landsat instruments, with the addition of two new spectral bands: a deep blue visible channel (band 1) specifically designed for water resources and coastal zone investigation, and a new infrared channel (band 9) for the detection of cirrus clouds. A new Quality Assurance band is also included with each data product. This provides information on the presence of features such as clouds, water, and snow.

The TIRS instrument collects two spectral bands for the wavelength covered by a single band on the previous TM and ETM+ sensors. The data quality (signal to noise ratio) and radiometric quantization (12-bits) of the OLI and TIRS is higher than previous Landsat instruments (8-bit for TM and ETM+), providing significant improvement in the ability to detect changes on the Earth's surface (http://landsat.usgs.gov/landsat8.php). Figure 2 shows a comparison of Landsat 8 and Landsat 7 spectral bands

In this study, four Landsat 8 images acquired on the 25th of June, the 29th of September, 2013 and the 3rd of January, the 24th of March, 2014 are used to represent the summer, autumn, winter and spring season, respectively. Among the 11 bands of Landsat 8, the OLI spectral bands 1 to 7 are chosen to generate land cover classification map of the study area because they have the same resolution of 30 meters and radiation information of bands 10 and 11 which provide metadata, such as thermal constant, rescaling factor value etc., used to estimate the temperature at the Earth's surface. Bands 4 and 5 are used to calculate Normalized Difference Vegetation Index (NDVI). Bands 2, 5 and 6 are applied to construct band combination in which the colours tell healthy vegetation information about the parts of the spectrum that are represented in RGB. Bands 10 and 11 are used to calculate land surface temperature.

Table 2: Spectral characteristics of Landsat 8.

(Source: http://landsat.usgs.gov/band_designations_landsat_satellites.php)

Band	Description	Wavelength (µm)	Resolution(meters)
1*	Coastal aerosol	0.43 - 0.45	30
2*	Blue	0.45 - 0.51	30
3*	Green	0.53 - 0.59	30
4*	Red	0.64 - 0.67	30
5	Near Infrared (NIR)	0.85 - 0.88	30
6	SWIR 1	1.57 - 1.65	30
7	SWIR 2	2.11 - 2.29	30
8*	Panchromatic	0.50 - 0.68	15
9	Cirrus	1.36 - 1.38	30
10**	Thermal Infrared (TIRS) 1	10.60 - 11.19	100 * (30)
11**	Thermal Infrared (TIRS) 2	11.50 - 12.51	100 * (30)

*Within the visible spectrum

** TIRS bands are acquired at 100 meter resolution, but are resampled to 30 meter in delivered data product.

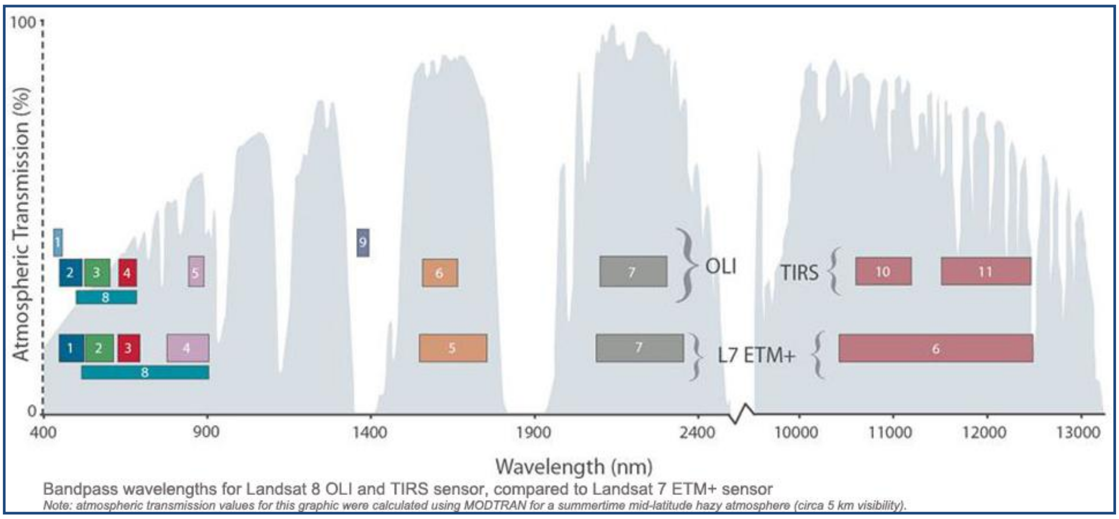

Figure 3: Bandpass wavelength for Landsat 8 OLI and TIRS sensors, compared to Landsat 7 ETM+ sensor. (Source: http://landsat.usgs.gov/L8_band_combos.php)

Satellite datasets of Landsat 8 over Xi'an city have been used in this study and can be downloaded from Glovis. The details of satellite data are presented below.

Landsat 8 data of :

- June 25, 2013 of WRS-2 Path/Row 127/36
- September 29, 2013 of WRS-2 Path/Row 127/36
- January 3, 2014 of WRS-2 Path/Row 127/36
- March 24, 2014 of WRS-2 Path/Row 127/36

These four Landsat 8 imageries represent the summer, autumn, winter and spring seasons respectively..

3. METHODS

This chapter can be summarised into 4 stages: data processing-Atmospheric correction, image classification, estimation of land surface temperature (LST) and statistic analysis.

Atmospheric correction - Atmospheric correction consists of software and module functions and determination of parameters. Some of the parameters are extracted from the metadata of downloaded Landsat 8 data and the remaining are estimated from the software.

Land cover classification phase includes two main steps: supervised classification, accuracy assessment.

The third stage mainly focuses on calculating land surface temperature (LST) using Split-Window (SW) Algorithm. In this algorithm, there are several parameters which are needed to determined.

3.1. Atmospheric correction of Landsat 8 images

Earth-observing satellite sensors map the earth's surface properties. However, the radiation of the objects recorded by the satellites are largely interacted with the effect of atmosphere, such as absorption and scattering of atmospheric particle and molecules (Mahiny & Turner, 2007). Meanwhile, haze from water vapour and aerosol particles influence the recorded signal(Tao et al., 2012). In addition, in rugged terrain, varying illumination conditions (sunny and shady hills) change the "true" spectral behaviour of surfaces.

Errors happened due to atmospheric effects influence the quality of the information extracted from remote measurement, such as vegetation indices (Courault et al., 2003). It is especially found that for the calculation of NDVI (Normalized Differential Vegetation Index), the effects of the atmosphere should be considered (Hadjimitsis et al., 2010). In this research, the purpose is to analyze the spatial pattern of green vegetation and its relationship with land surface temperature. Therefore, the processing of atmospheric correction is absolutely necessary before carry through the research questions.

ATCOR for ERDAS IMAGINE is a professional atmospheric correction and de-hazing tool developed by DLR (German Aerospace Centre) with the objective to reduce haze content and eliminate atmospheric and terrain effects to retrieve physical parameters of the earth's surface, including surface reflectance, ground visibility and temperature (Source: http://www.geosystems.de/atcor/). Such correction is especially important in cases where multi-temporal, multi-sensor or multi-condition images are to be compared and analyzed.

ATCOR for IMAGINE consists of two options: ATCOR 2 and ATCOR 3. ATCOR 2 is used for atmospheric correction in flat terrain (the "2" stands for "2 dimensions"). ATCOR 3 is used for atmospheric correction in rugged terrain by integrating a DEM (the "3" stands for "3 dimensions") (R & D.Schlapfer, 2014). In this research, the terrain of the study area is flat. Thus ATCOR2 is chosen to conduct the atmospheric correction.

ATCOR uses a "Project File" which stores all information gathered during operation. In the atmospheric correction parameters, some can be extracted from satellite imagery metadata. The other parameters are estimated and calculated using ATCOR software. In ATCOR 2, a number of important inputs are drawn below (Table 3):

- An information (acquisition date, input layers and sensor type) about input raster file;

- An accurate radiometric calibration is required, which shows the knowledge of c_0, c_1 in each spectral band (see Table 4). It is obtained from the metadata of satellite imagery data;
- A valid solar zenith of the sun at the recording time for the given location. It can be calculated from ATCOR 2 with information of the time of day (UTC), day of month, month of year, longitude and latitude. Also the solar zenith can be calculated using sun elevation. These detailed values are all from the metadata of imagery;
- An accurate estimate of the main atmospheric parameters (aerosol type, visibility or optical thickness) is necessary, because these influence the value of path radiance, transmittance. The aerosol type includes the absorption and scattering properties of the particles, and wavelength dependence of the optical properties. ATCOR supports four basic aerosol types: rural, urban, maritime, and desert. The decision are made based on the geographic location. In this study area, urban aerosol type is assumed because the urban areas in the satellite image need atmospheric correction and haze remove most.

Table 3: Input parameters in the ATCOR 2 module

Parameters	**Description**
Input raster file	The image has to be corrected, the input-file source
Input layers	Selection of spectral bands to be corrected
Sensor	Satellite sensor: Landsat-8 OLI
Calibration file	The sensor specifications (Table 4)
Solar zenith	Obtained from metadata
Visibility	The scene visibility for the aerosol model (km)
Model for solar region	"Urban" is selected according to the atmospheric condition of study. The atmospheric model: midlat_summer_urban, fall_(spring)_urban and midlat_winter_urban are chosen for summer, autumn & spring and winter respectively.

Table 4: The c_0 and c_1 coefficients of bands 1-7 for Landsat 8 image of June 25, 2013.

7	c_0	c_1 [mW/cm^2 sr micron]
1	-6.076628	0.001215
2	-6.222541	0.001245
3	-5.734018	0.001147
4	-4.835247	0.000967
5	-2.95893	0.000592
6	-0.735859	0.000147
7	-0.248024	0.000050

Before atmospheric correction, the NDVI values were in range of -0.065 to 0.375 while after applying the atmospheric correction, the dynamic range of NDVI map changes to -0.289 to 0.692. Figure 4 shows NDVI maps of Landsat 8 data before and after atmospheric correction. The image clearly shows that the overall range of NDVI has been adjusted.

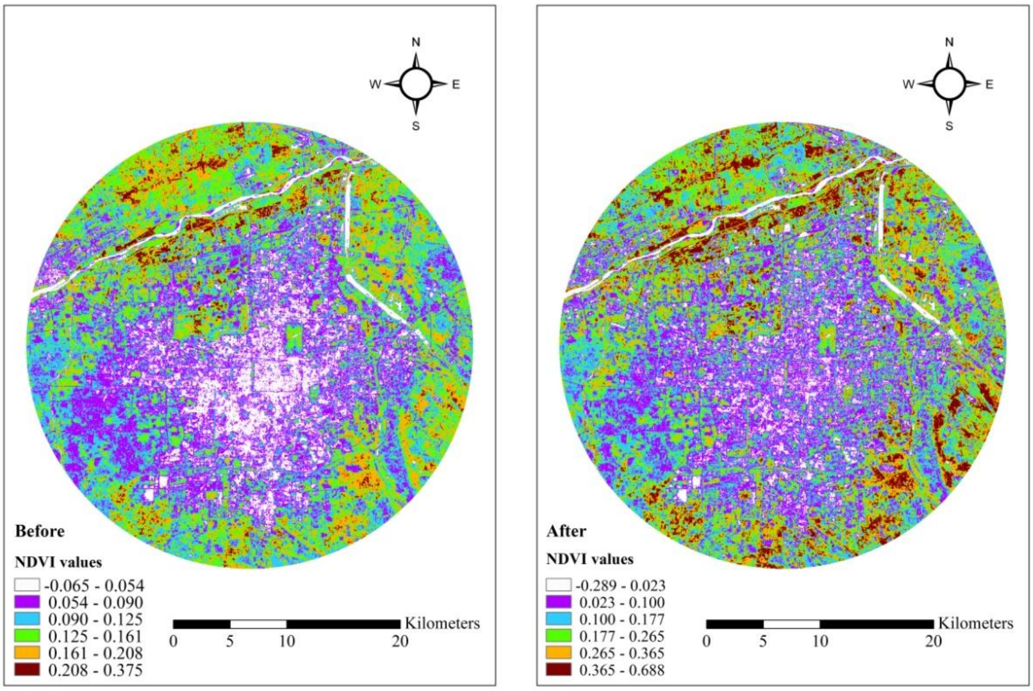

Figure 4: Comparison of NDVI maps before and after atmospheric correction, dated 29th September 2013

Table 5 and Table 6 clearly depict the overall NDVI values and NDVI values for each land cover type before and after atmospheric correction in the four seasons.

Table 5: The range of NDVI values before and after atmospheric correction for four seasons.

Image (Season)	Before	After
June 25, 2013 (Summer)	-0.180 to 0.589	-1 to 1
September 29, 2013 (Autumn)	-0.065 to 0.375	-0.286 to 0.688
January 3, 2014 (Winter)	-0.124 to 0.297	-1 to 1
March 24, 2014 (Spring)	-0.118 to 0.397	-0.486 to 0.963

Table 6: Comparisons between NDVI values for four land cover type before and after atmospheric correction in four seasons.

Image (Season)	Land cover type	Before	After
June 25, 2013 (Summer)	Water	0.031	-0.197
	Built-up	0.148	0.204
	Green-Vegetation	0.317	0.577
	Bare land	0.153	0.185
September 29, 2013 (Autumn)	Water	0.006	-0.085
	Built-up	0.076	0.086
	Green-Vegetation	0.146	0.275
	Bare land	0.099	0.126
January 3, 2014 (Winter)	Water	-0.042	-0.202
	Built-up	0.023	0.042
	Green-Vegetation	0.100	0.315
	Bare land	0.051	0.130
March 24, 2014 (Spring)	Water	-0.030	-0.159
	Bare land	0.060	0.076
	Green-Vegetation	0.159	0.323
	Bare land	0.075	0.110

3.1. Land cover classification and accuracy assessment

Different image classification procedures can be used for different purposes, which are generally grouped into unsupervised and supervised classifications (Srivastava et al., 2012). In an unsupervised classification the image is classified by aggregating image data into natural spectral groups or clusters (Tursilowati et al., 2012). While in the supervised classification approach, first the training sets are created and then classification steps are executed .

Unsupervised classification is useful for evaluating areas where you have little or no knowledge about the study area. It has few disadvantages where the lack of information about a scene can make the algorithm decisions difficult and separate pixels with slightly different spectral values mistakenly and assign them to a unique cluster when they, in reality, represent a spectral continuum of a group of similar objects (Asmat et al., 2003). However, in the method of supervised classification, it uses pixels of known classes to identify pixels of unknown classes. Besides operator can detect errors and often remedy them. In this study, supervised classification method is applied to generate land cover maps of the four scenes.

Commonly, used supervised classification approaches are parallelepiped, minimum distance to mean and maximum likelihood. Among these algorithms, the maximum likelihood method is generally preferred due to its higher accuracy levels (Asmat et al., 2003). Maximum likelihood classification is derived from the Bayes theorem, which based on the assumption that the probability distribution for each spectral class is of the form of a multivariate normal model with dimensions which equal the number of spectral bands (Jia & Richards, 1994). It makes use of a discriminated function to assign a pixel to the class with the highest likelihood (Ahmad & Quegan, 2012).

In this study, the object of attention is seasonal spatial patterns of green vegetation in rural areas and its relationship with urban heat islands effect. Therefore, the land cover is going to be classified into 4 categories: green-vegetated areas (including agricultural land, forests and grassland), built-up areas (including roads and railways), water and bare land.

In the procedure of identifying training sets, the sample points (region of interest) are selected by visual interpretation, consulting with the high resolution aerial images and photographs from Google Earth, NDVI maps in four seasons, local knowledge of study area and information from band combinations (R,G,B:5,6,2,) applied to Landsat 8 (shown in Figure 5, 6 and 7). Then the selected points were divided into a training subset (60%) and a testing subset (40%) by random sampling, for the purpose of independent training and accuracy assessment. Table 7 shows the number of sample points of each land cover category in four seasons.

Table 7: The number of sample points of land cover types in four seasons.

Image(season)	Water	Built-up	Green-vegetation	Bare land
June 25, 2013 (Summer)	37	35	47	40
September 29, 2013 (Autumn)	36	41	50	34
January 3, 2014 (Winter)	33	42	40	33
March 24, 2014 (Spring)	36	35	36	32

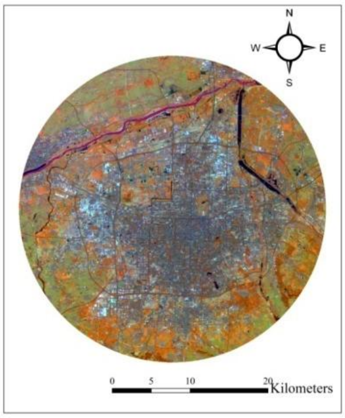

Figure 5: Band combination applied, dated 25th June, 2013 (R,G,B: 5,6,2,)

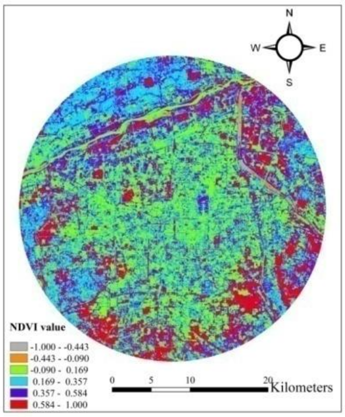

Figure 6: NDVI map for Landsat 8 data, dated 25th June, 2013.

Figure 7: High resolution aerial image of the study area, data from Google Earth.

Accuracy assessment is an important part to analyze the result of the classified image through the overall accuracy and Kappa coefficient. The confusion matrix is used for a quantitative analysis of the land cover classification accuracy and the reference data are the remaining of 40% sample points.

Furthermore, one of the most widely applied approach of comparing accuracy in remote sensing is the comparison of kappa coefficients, the statistical significance of the difference between two independent kappa coefficients derived from different classification results is evaluated by the Z-test value (Foody, 2009). The hypothesis is that two Kappas are equal. If final Z value is greater than a certain value (1.96 for 95% confidence level test), it indicates that the two compared classifications are significantly different at the 5% significance level. (Congalton & Green, 2002).

Additionally, a suitable enhancing filtering is carried out after the classification process on the produced thematic map to improve the image visual interpretability. Classic pixel-based classification method often leads to the "salt and pepper" effects in the final classification map, derived from the isolated pixels of the one class within another dominant class (Al-Fares, 2013). To improve the classification results, the majority mode filter in ENVI is used as a post-classification procedure. In this study, the Kernel size of 3 x 3 is applied to smooth the appearance of the image.

In order to quantify the spatial patterns of green-vegetated areas, 5 buffer zones were created across the study area. The city centre acts as a centre point to create buffer zone. (shown in Figure 8). As the radius of the study area is 20 km. The buffer zones are equally distributed into 5 zones, which are 0-4, 4-8, 8-12, 12-16, and 16-20 km in distance from city centre, respectively. These buffer zones were applied to explain the spatial pattern of green-vegetation areas and also used to quantify the spatial patterns of urban heat island phenomenon (Weng et al., 2004).

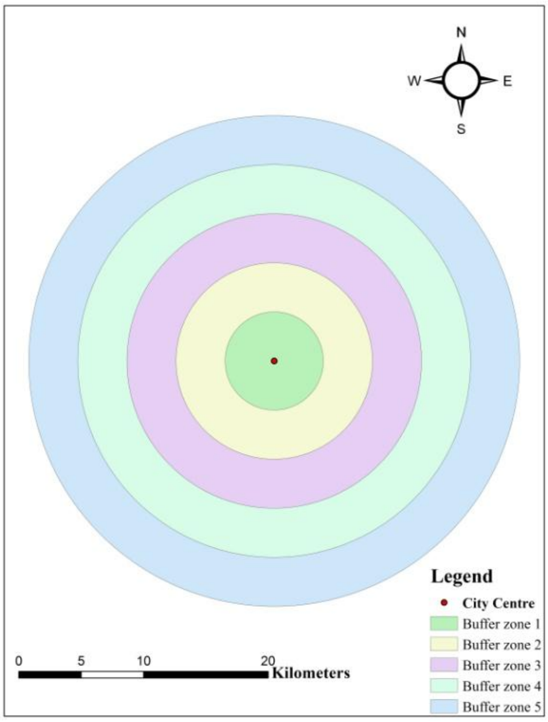

Figure 8: Five buffer zones drawn in the study area.

The whole image classification section are conducted by software ENVI and ArcGIS 10.2.1. Detailed results are showed in Chapter 4.

3.2. Calculating land surface temperature from Landsat 8 images

Land surface temperature (LST) is the temperature emitted by surface and measured in Kelvin (Rajeshwari & Mani, 2014) and is a good indicator of energy and water balance at the land-atmosphere interface (Yu et al., 2008). It can be estimated from satellite remote sensing and retrieved from TIR data (Jiménez-muñoz et al., 2014).

There are several algorithms dealing with estimating LST data, such as Split-Window (SW), Dual-Angel (DA), Single-Channel (SC), Sobrino and Mao (Rajeshwari & Mani, 2014). For Landsat 8, since the formal single band has been split into two TIR bands, the bandwidths of TIRS bands are narrowed, the use of two separate bands can minimize the error in the retrieval of LST (Caselles et al,, 1998). Hence, the present two TIR bands open a possibility to apply split-window (SW) algorithms, which corrects for atmospheric effects based on the differential absorption in adjacent infrared bands (Wan et al., 1996), instead of single-channel (SC) algorithms to retrieval LST (Jiménez-muñoz et al., 2014).

In this research, SW algorithm is chosen to calculate land surface temperature and two thermal bands 10 and 11 are used in algorithm. For inversion of LST from remote sensing data, it is required to correct atmosphere-induced effects, that is the absorption and emission of atmospheric water vapour and land surface emissivity (LSE) (Zhao et al., 2005). Thus the inputs for SW algorithm are not only brightness temperatures (Rajeshwari & Mani, 2014), but also water vapour content and land surface emissivity (LSE).

In this section, there are four steps to estimate land surface temperature using ArcGis software : conversion of digital numbers to TOA radiance value, conversion of TOA radiance value to brightness temperature, estimation of land surface emissivity and calculate land surface temperature. They are described as below.

3.2.1. Conversion of digital numbers (DN) to TOA radiance value

The brightness temperature can be obtained using data from the Landsat 8 TIRS instrument. First, convert Digital Numbers (DN) to Top-of-Atmosphere (TOA) radiance values.

Landsat TIRS bands data can be converted to TOA planetary reflectance using reflectance rescaling coefficients (Table 8) provided in the product metadata file (MTL file). The following equation is used to convert DN values to TOA reflectance for OLI data as follows:

$$L_\lambda = M_L Q_{cal} + A_L \qquad \text{(Equation 1)}$$

Where,

L_λ = TOA spectral radiance (Watts/(m2 * srad * μm))

M_L = Band-specific multiplicative rescaling factor from the metadata (RADIANCE_MULT_BAND_x, where x is the band number)

A_L = Band-specific additive rescaling factor from the metadata (RADIANCE_ADD_BAND_x, where x is the band number)

Q_{cal} = Quantized and calibrated standard product pixel values (DN)

Table 8: Landsat 8 reflectance rescaling coefficients for band 10 and band 11.

Rescaling Factor	Band 10	Band 11
M_L	0.000342	0.000342
A_L	0.1	0.1

3.2.2. Conversion of TOA radiance values to brightness temperature

After conversion of digital numbers to TOA radiance, the next step is converting the TOA radiance values to TOA brightness temperature in Kelvin. TIRS bands data can be converted from spectral radiance to brightness temperature using the thermal constants (Table 9) provided in the metadata file (MTL file):

$$T = \frac{K2}{Ln\left(\frac{K1}{L\lambda}+1\right)} \qquad \text{(Equation 2)}$$

Where,

T = At-satellite brightness temperature (Kelvin)

L_λ = TOA spectral radiance (Watts/(m2 * srad * µm))

K_1 = Band-specific thermal conversion constant from the metadata (K1_CONSTANT_BAND_x, where x is the band number, 10 or 11)

K_2 = Band-specific thermal conversion constant from the metadata (K2_CONSTANT_BAND_x, where x is the band number, 10 or 11)

Table 9: Landsat 8 thermal constants for band 10 and band 11.

Thermal Constant	Band 10	Band 11
K_1	1321.08	1201.14
K_2	777.89	480.89

3.2.3. Estimation of land surface emissivity

For Landsat images, land surface emissivity is mainly determined by the surface materials and the range of bands. In this study, the land surface emissivity is estimated using NDVI threshold method which uses information collected by OLI in VNIR bands (reflectance or vegetation indices) depending on the fractional vegetation cover for a given pixel (Qin et al., 2006).

As emissivity of different land cover types varies significantly, the land cover classification maps are used to estimate land surface emissivity. Generally, there are mainly four types of land feature on earth: water, built-up, soil and vegetation. For the bands 10 and 11 in Landsat 8, the emissivity of each land feature is set according to Aster Spectral Library (http://speclib.jpl.nasa.gov/). The detailed emissivity values are presented in Table 10.

Table 10: Emissivity values for different typical land feature in Landsat 8.

Bands	Land feature	Emissivity value (ε)
Band 10	Water (w)	0.99683
	Built-up (b)	0.964885
	Soil (s)	0.96767
	Green-Vegetation (v)	0.98672
Band 11	Water (w)	0.99254
	Built-up (b)	0. 975115
	Soil (s)	0.97790
	Green-Vegetation (v)	0.98990

However, it's hard to find 100% vegetation, bare land and built-up surface and at the pixel scale, the variation of emissivity is along with natural surface heterogeneity. Besides, the emissivity is largely related to the nature of vegetation cover, the surface roughness etc. In this research, one attempt has been conduct to estimate emissivity by using the proportion of vegetation cover in each pixel. For four land cover types, the emissivity values of water in two bands 10 and 11 are 0.99683 and 0.99254, separately and the estimation of emissivity for built-up, vegetation and others are mixed pixels analysis which are described below.

For natural land surface, the pixel of natural surface can be simply treated as a mixture of vegetation and soil. Therefore, emissivity calculation for vegetation and others can follow below Equation 3.3 used for mixture pixel which contains vegetation and soil:

$$\varepsilon_i=P_v R_v \varepsilon_{iv}+(1-P_v)R_s\varepsilon_{is} + d\varepsilon \qquad \text{(Equation 3)}$$

Where,

ε_i = Land surface emissivity for band i in Landsat 8 (i = 10, 11)

P_v = Fractional vegetation cover, defined as $(NDVI-NDVI_s)/(NDVI_v-MDVI_s)$, and $NDVI_s$ and $NDVI_v$ are NDVI threshold for vegetation and others;

$d\varepsilon$ = Thermal radiation interaction correction value

- When $P_v < 0.5$, $d\varepsilon=0.0038P_v$ (Equation 4)
- When $P_v > 0.5$, $d\varepsilon=0.0038(1-P_v)$ (Equation 5)
- When $P_v = 0.5$, $d\varepsilon=0.0019$ (Equation 6)

R_v = Temperature ratio for vegetation

R_s = Temperature ratio for soil

R_v and R_s calculation algorithms are described later.

However, for 100% vegetation or bare land areas, the land surface emissivity can be represented using typical vegetation or bare land surface emissivity (showed in Table 9).

For land cover type built-up, it is a mixture of built-up and vegetation. The calculation equation of emissivity is as below:

$$\varepsilon_i = P_v R_v \varepsilon_{iv} + (1-P_v) R_b \varepsilon_{ib} + d\varepsilon \quad \text{(Equation 7)}$$

Where,

ε_i = Land surface emissivity for band i in Landsat 8 (i = 10, 11)

P_v = Fractional vegetation cover, defined as ($NDVI-NDVI_s$)/($NDVI_v-MDVI_s$), and $NDVI_s$ and $NDVI_v$ are NDVI threshold for vegetation and others;

$d\varepsilon$ = Thermal radiation interaction correction value

R_v = Temperature ratio for vegetation

R_b = Temperature ratio for built-up

For temperature ratio R_v , R_s and R_b , they are defined as Ri=(Ti/T)4 (i=vegetation , soil and built-up). In this study, the estimation of temperature ratio for vegetation, soil and built-up are showed below:

$$R_v = 0.9332 + 0.0585\, P_v \quad \text{(Equation 8)}$$

$$R_s = 0.9902 + 0.1068\, P_v \quad \text{(Equation 9)}$$

$$R_b = 0.9886 + 0.1287\, P_v \quad \text{(Equation 10)}$$

3.2.4. Land surface temperature

In the Split-Window (SW) Algorithm (Equation 3.10), the inputs are brightness temperatures for band 10 and band 11, land surface emissivity, water vapour content and c0-c6 coefficients.

$$T_s = T_i + c_1(T_i - T_j) + c_2(T_i - T_j)^2 + c_0 + (c_3 + c_4 w)(1 - \varepsilon) + (c_5 + c_6 w)\Delta\varepsilon \quad \text{(Equation 11)}$$

where,

Ti(j) = At-sensor brightness temperatures for band i(j), i=10 and j=11 (Kelvin)

ε = Mean emissivity, defined as $\varepsilon = 0.5\,(\varepsilon i + \varepsilon j)$

$\Delta\varepsilon$ = Emissivity difference, defined as $\Delta\varepsilon = (\varepsilon i - \varepsilon j)$

w = Atmospheric water vapor content ($g \cdot cm^{-2}$)

c_i = Coefficients for the SW algorithm, i=0 to 6, determined from simulated data (Table 11)

The atmospheric water vapour content can be derived from local measurements in-situ or nearby meteorological stations (Rozenstein et al., 2014). However, it is hard to get the real water vapour content per pixel, the parameter in this study are set as a constant according to local meteorology.

In order to describe the spatial patterns of land surface temperature in four seasons, the five buffer zones created in section 3.1. are applied to quantify the spatial distributions.

Table 11: Coefficients for the Split-Window Split-Window (SW) algorithm

Coefficients	Values
C_0	-0.268
C_1	1.378
C_2	0.183
C_3	54.30
C_4	-2.238
C_5	-129.20
C_6	16.40

3.3. Statistical analysis

This section is to examine the relationships between spatial patterns of green-vegetated areas and urban heat islands in four seasons.

Firstly, the proportion of green-vegetated area and bare land in each buffer zone is calculated. The former is tested by Z-test to know whether the proportion of green vegetation in each buffer zone is significantly different from each other. It shows the spatial distribution of green vegetation and explaining how the green vegetation changes with the increasing distance from city centre in four seasons.

Secondly, in the phenomenon of urban heat island, the main focus is on the temperature in urban areas where the built-up areas occupy most land. Therefore, the significant differences of land surface temperature only in built-up areas among buffer zones are tested in this step. In each buffer zone, sample points (shown in Table 12) are randomly selected in built-up areas and for each sample point the corresponding land surface temperature value is extracted. One-way ANOVA and Kruskal-Wallis test are used to determine whether the differences between the land surface temperature in each buffer are statistically significant. Before using these two statistical tests, normality test is necessary to check whether the sample data are normally distributed. If the data are not normal distributed, the Kruskal-Wallis test is applied (McDonald, 2014). The Kruskal-Wallis test is a nonparametric test used to compare three or more groups. It is used to test the null hypothesis that all populations have identical distribution functions. It is the non-parametric version of ANOVA and a generalized form of the Mann-Whitney test method because it permits 2 or more groups. Once determining that statistically significant differences exist among groups, Mann-Whitney U test is applied as post hoc test to examine which groups are different from each other.

If the data are normal distribution, using one-way ANOVA to test for differences in the means of the dependent variable broken down by the levels of the independent variable (Rutherford, 2001). However, one assumption is needed to accept to make sure the result is valid, that is there needs to be homogeneity of variances. If the data can met this assumption, once determining that differences exist among the means, post hoc range tests (Scheffe post-hoc test) and pair wise multiple comparisons can determine which means differ statistically. If data does violate this assumption, a Welch ANOVA, as well as alternative post-hoc tests (Games-Howell test instead of Scheffe post-hoc test) will be applied.

Thirdly, in order to investigate the effect of green vegetation on the urban heat islands, the significant differences of land surface temperature among buffer zones are tested here. The statistical test method are the same as the second step, the number of sample points are 30, 90, 150, 210 and 270 corresponding to buffer 1 to 5, respectively. The number is decided by the areas of each buffer.

Generating random sample points for built-up is conducted in ArcGis 10.2.1, and statistical analysis is done with SPSS 22.

Table 12: The number of sample points in built-up areas , in each buffer zone for the four seasons.

The number of Sample points	Buffer 1	Buffer 2	Buffer 3	Buffer 4	Buffer 5
Summer	30	80	80	80	75
Autumn	30	80	100	95	85
Winter	30	77	100	75	60
Spring	30	80	115	80	50

4. RESULTS

This chapter shows the results according to the objectives of the research which are: (1). to quantify spatial and temporal patterns of green-vegetated areas in and around Xi'an City; (2). to estimate and explore spatial and temporal patterns of land surface temperature in and around Xi'an City; (3).Furthermore, relationship between the land surface temperature of each land cover type with the spatial distribution of green-vegetated areas are analyzed.

4.1. Spatial patterns of green-vegetated areas in four seasons

4.1.1. Land cover maps and accuracy assessment

Figure 9 shows the classified land cover maps of the study area through maximum likelihood classification approach. From the four maps, it is revealed that the spatial patterns of vegetation changes seasonally. During summer, the green vegetation mainly located around built-up areas and very few in the city (Figure 9 (a)). The area of green vegetation is highest in autumn compared to other seasons (Figure 9 (b)). Through visual interpretation, the distribution pattern of vegetation in autumn is similar to summer but the density of green vegetation is higher in autumn compared to summer. In winter (Figure 9 (c))., bare land is dominant land cover type around the city, while the area of green vegetation is least of all four seasons, distributed mainly away from built-up areas. In spring (Figure 9 (d))., the area of green vegetation is higher than in winter but lower than in summer.

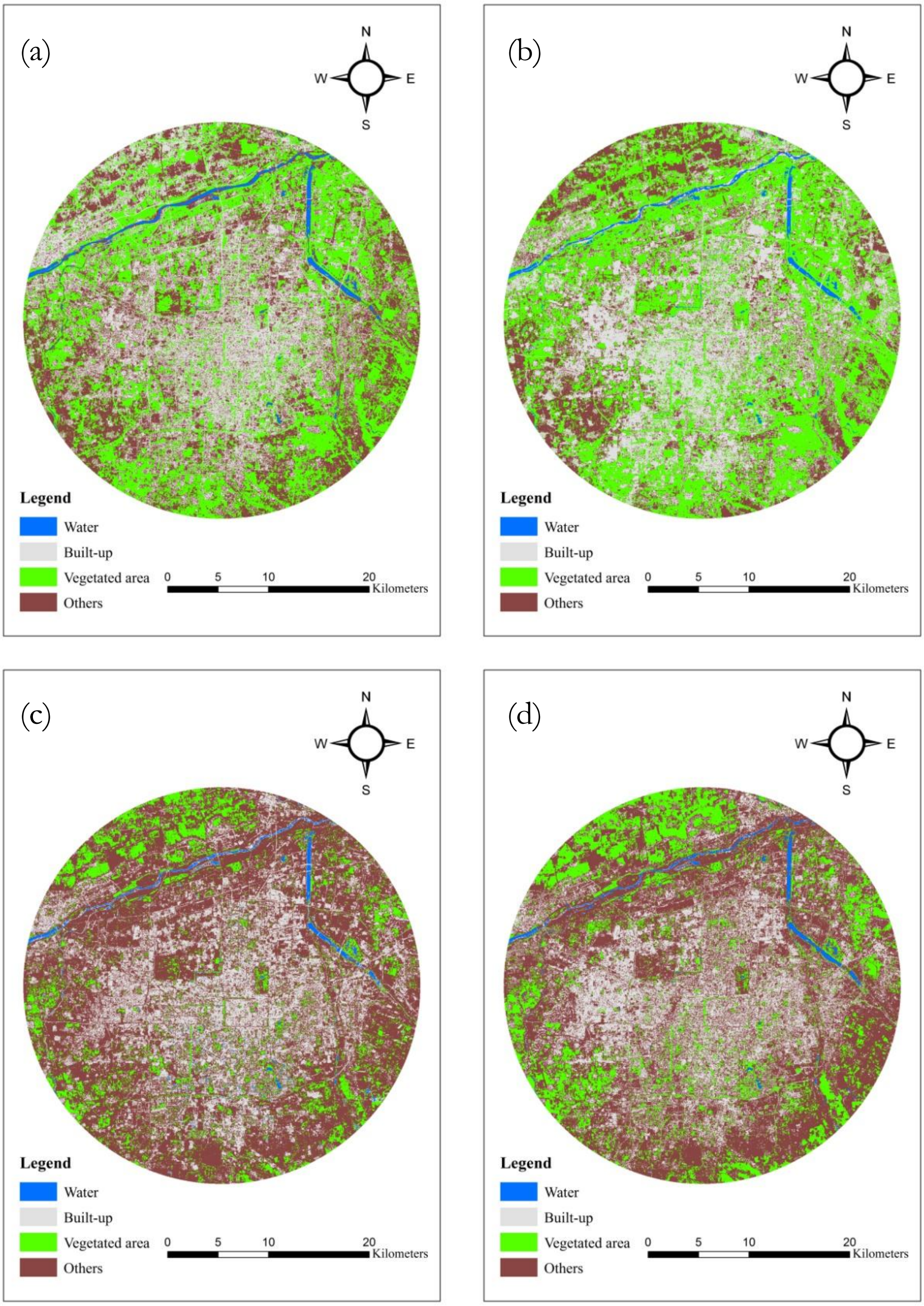

Figure 9: Land cover classification maps: (a) summer; (b) autumn; (c) winter; (d) spring.

For each image classification, the accuracy assessment includes an overall accuracy and Kappa statistical analysis. Table 13 shows the confusion matrixes of four images.

Table 13: Confusion matrix for accuracy assessment in four season images.

Images	Class	Ground Reference Data						
		Water	Built-up	Green-vegetation	Others	Total	Producer's Accuracy (%)	User's Accuracy (%)
summer	Water	13	0	0	0	13	86.67	100.00
	Built-up	0	11	0	0	11	78.57	100.00
	Green vegetation	0	0	19	0	19	100.00	100.00
	Others	2	3	0	16	21	100.00	76.19
	Total	15	14	19	16	64	Overall Accuracy: 92.19%	
autumn	Water	12	0	0	0	12	85.71	100
	Built-up	1	14	0	3	18	87.50	77.78
	Green vegetation	1	0	20	0	21	100	95.24
	Others	0	2	0	11	13	78.57	84.62
	Total	14	16	20	14	64	Overall Accuracy: 89.06%	
winter	Water	12	1	0	0	13	97.31	92.31
	Built-up	1	15	0	2	18	88.24	83.33
	Green vegetation	0	0	16	0	16	100.00	100.00
	Others	0	1	0	11	12	84.62	91.67
	Total	13	17	16	13	59	Overall Accuracy: 91.53%	
spring	Water	11	0	0	0	11	78.57	100.00
	Built-up	2	13	0	0	15	92.86	86.67
	Green vegetation	0	0	14	0	14	100.00	100.00
	Others	1	1	0	13	15	100.00	86.67
	Total	14	14	14	13	55	Overall Accuracy: 92.73%	

Table 14 shows the overall accuracy assessment for the four land cover classification maps representing summer, autumn, winter and spring is 92.19%, 89.06%, 91.53% and 92.73%, respectively. The accuracy of the four land cover classification maps is similar, as is also the Kappa coefficient.

Table 14: Accuracy assessment of classified Landsat 8 images for four seasons.

Image (Season)	Overall accuracy	Overall Kappa coefficient
June 25, 2013 (Summer)	92.19%	0.90
September 29, 2013 (Autumn)	89.06%	0.85
January 3, 2014 (Winter)	91.53%	0.89
March 24, 2014 (Spring)	92.73%	0.90

Also, a Z-test is performed to test the statistical significance of the difference between two independent Kappa coefficients as displayed in Table 15. It shows that the Z-values are less than 1.96 for 95% confidence level test. Therefore, the null hypothesis i.e. two Kappas coefficient are equal, is accepted. That means there are no significant difference at the 5% significance level among the Kappas of the four images and the land cover classification of the four images is accurate.

Table 15: The result of Z-test for Kappas.

Images	Summer	Autumn image	Winter image	Spring image
Summer	——			
Autumn image	0.83	——		
Winter image	0.18	0.64	——	
Spring image	0.17	0.97	0.33	——

4.1.2. Quantification of spatial patterns in green vegetation areas.

In order to quantify the spatial patterns of green vegetation, five buffer zones were created. In each buffer zone, the area proportion of green vegetation is calculated (see in Table 16). In all seasons the area of green vegetation increases with increasing distance from the city centre. Comparing the four seasons, in autumn, the area of green vegetation in each buffer zone is largest, whereas in winter, the area is smallest. Figure 10 also shows the change of green vegetation areas in each buffer zone and trend lines to describe the degree of changes within the buffers. In summer, the vegetation areas are nearly the same in buffer 1 and buffer 2, and then increase gently from 26.22% to 41.99% within buffer 3 to buffer 5. In autumn, the trend line shows that from buffer 3 to buffer 5, the increase of area in vegetation is gradual and the slope of the trend line is similar to that in summer, which means in autumn and summer, the growth rate of green vegetation area are approximately the same, but the overall vegetation cover in autumn is higher. In winter, the proportion of green vegetation areas within buffer 1 to buffer 3 is similar , while in buffer 4 and 5, there are more proportion of green vegetation areas which increase from 8.06% to 17.16%. In spring, comparing to winter, the vegetation area in buffer 3 to 5 get larger (9%-26.84%) and there is more green vegetation around the urban areas.

The proportion of bare land is also shown in Table 16 and Figure 11. The areas of bare land is generally increasing from city centre to rural areas. Especially in winter the total area is largest of all four seasons, in all buffer zones. In autumn, the areas of bare land is least in each buffer. And also the proportion of green vegetation is higher than of bare land. In summer, the proportion of vegetation areas and bare land are approximately the same in all buffer zones. In spring and winter the proportion of bare land is higher than of green vegetation, in all buffer zones.

Table 16: Area proportion of green vegetation and bare land in five buffer zone, four seasons.

Summer	Buffer Area (km²)	Proportion	
		Green Vegetation (%)	Bare land (%)
Buffer 1	48.74	17.46	16.10
Buffer 2	146.23	18.70	21.66
Buffer 3	243.72	26.22	27.60
Buffer 4	341.21	37.17	34.56
Buffer 5	438.70	41.99	38.52

Autumn	Buffer Area (km²)	Proportion	
		Green Vegetation (%)	Bare land (%)
Buffer 1	48.74	26.98	8.67
Buffer 2	146.23	28.04	12.62
Buffer 3	243.72	38.68	16.33
Buffer 4	341.21	45.68	21.92
Buffer 5	438.70	47.59	31.39

Winter	Buffer Area (km²)	Proportion	
		Green Vegetation (%)	Bare land (%)
Buffer 1	48.74	5.37	40.77
Buffer 2	146.23	4.93	49.01
Buffer 3	243.72	5.16	59.14
Buffer 4	341.21	8.06	70.13
Buffer 5	438.70	17.16	70.35

Spring	Buffer Area (km²)	Proportion	
		Green Vegetation (%)	Bare land (%)
Buffer 1	48.74	6.49	45.89
Buffer 2	146.23	7.28	46.03
Buffer 3	243.72	9.00	53.48
Buffer 4	341.21	13.47	65.72
Buffer 5	438.70	26.84	63.65

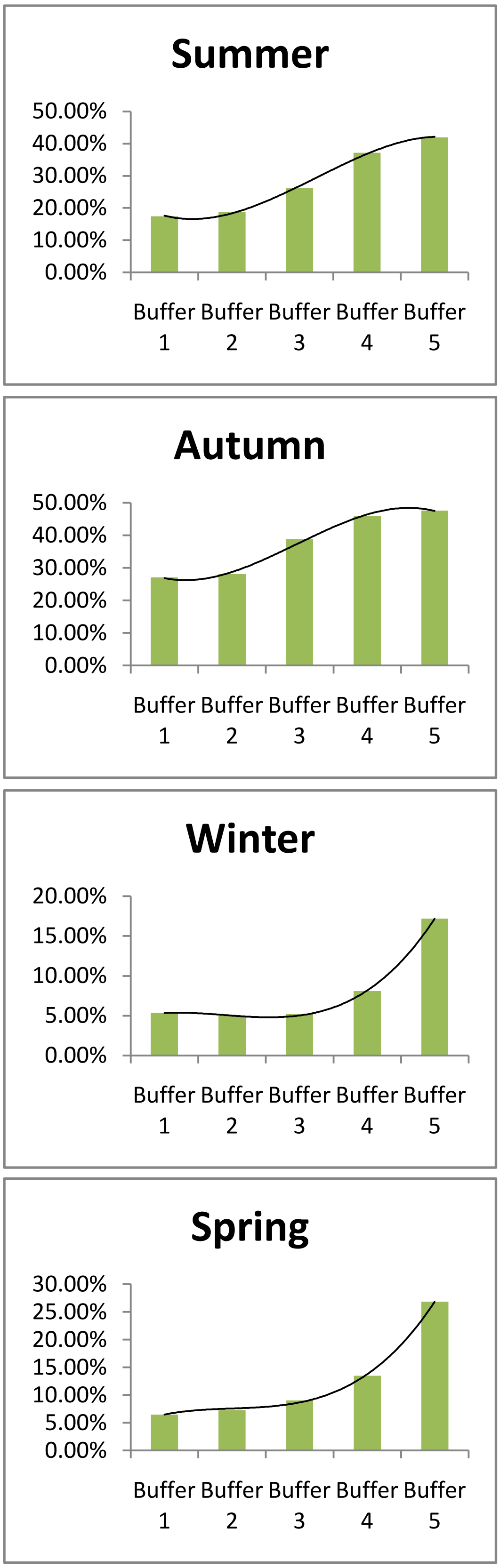

Figure 10: Area proportion of green vegetation in each buffer zone, four seasons.

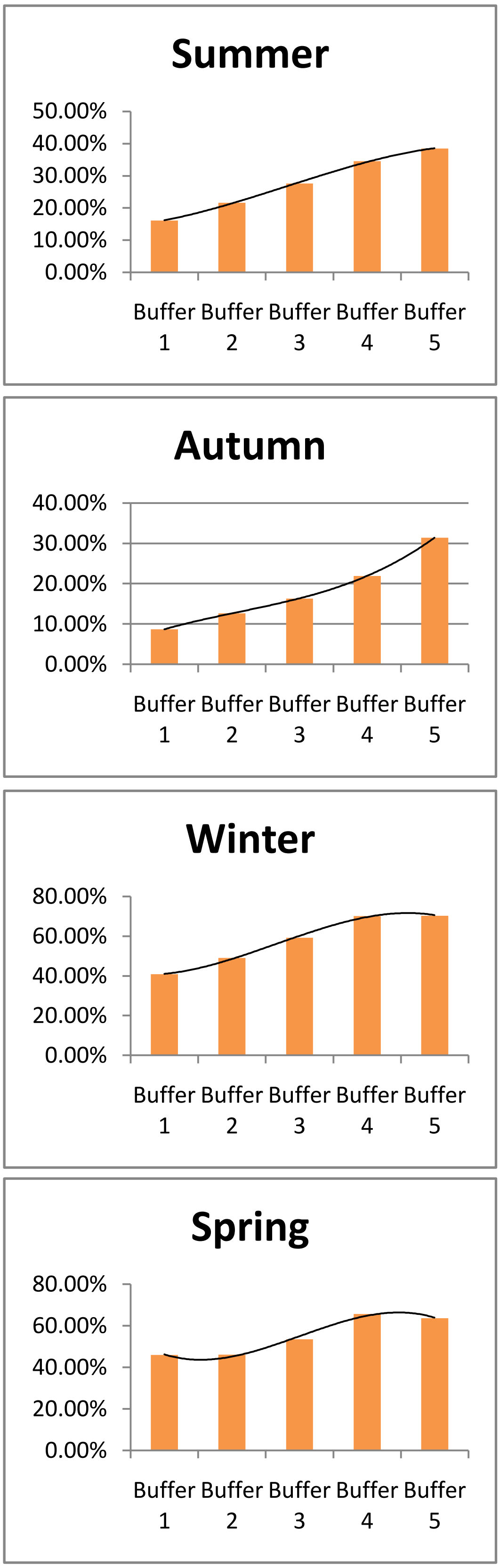

Figure 11: Area proportion of bare land in each buffer zone, four seasons.

4.2. Spatial patterns of land surface temperature in four seasons

4.2.1. Land surface temperature maps

Calculating land surface temperature uses Split-Windows (SW) algorithm, which contains two bands 10 and 11 of Landsat 8 thermal channel (10.6 - 11.19 and 11.5 to 12.51) in order to give more accuracy. In Figure 12 the land surface temperature in the four seasons is presented. In this figure, the legend used are range from the lowest land surface temperature and highest land surface temperature in four seasons. Therefore, it is more easy to find the land surface temperature for the four seasons intuitively. More red represents higher temperature and green means lower temperature. This figure shows that in summer, the land surface temperature is highest of all four seasons and in winter, the land surface temperature is lowest. The land surface temperature in autumn is nearly the same as in spring.

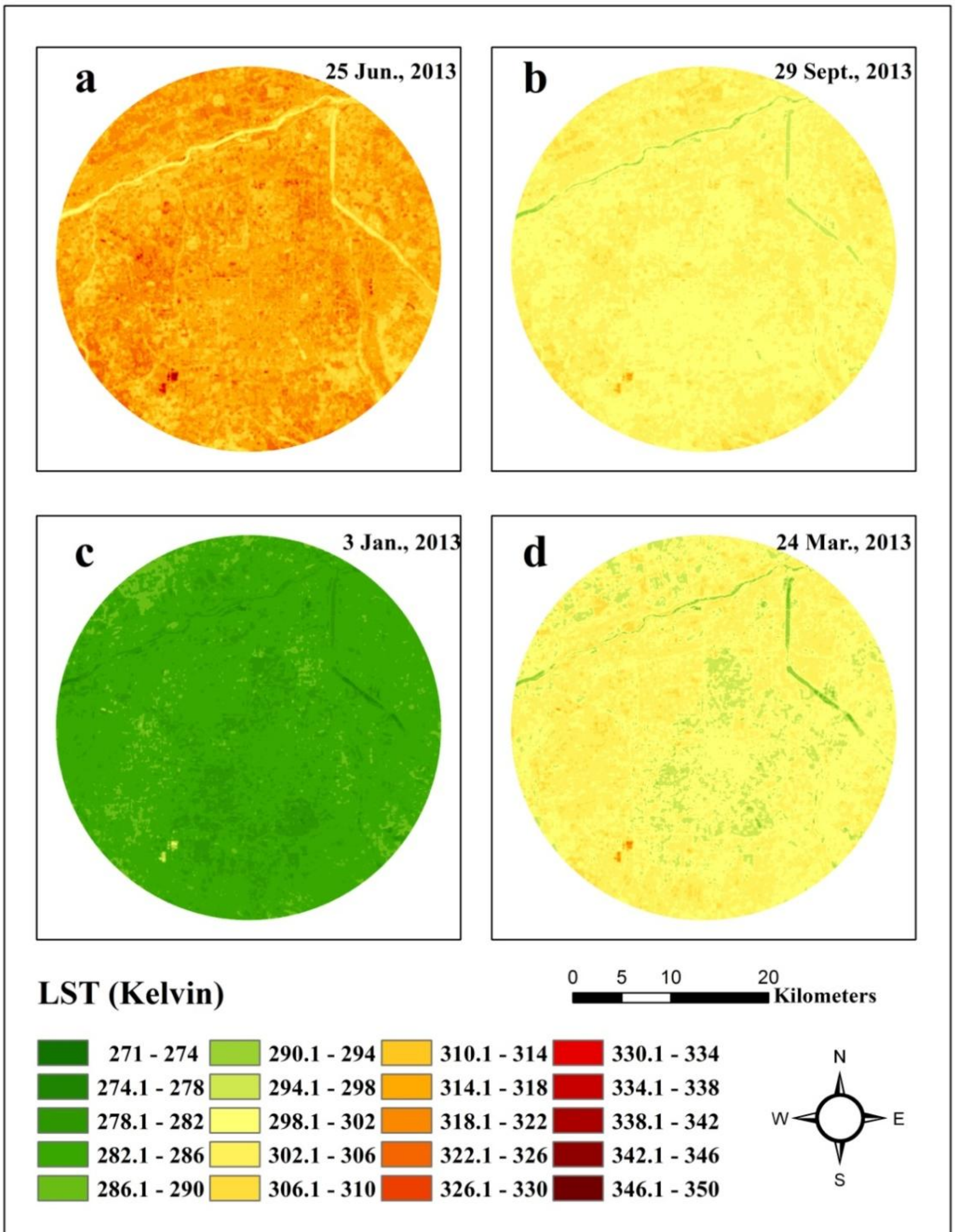

Figure 12: Normalized land surface temperature in summer (a), autumn (b), winter (c) and spring (d).

Figure 13 illustrates more details about the land surface temperature maps for the four seasons.

In summer (Figure 13 (a)), the land surface temperature ranges from 299.25 to 347.17 Kelvin with a mean of 315.97 Kelvin. The lower temperatures happen in water and green vegetation areas, and highest temperature zone mostly happens in bare land which surrounds urban areas. The land surface temperature in built-up is lower than that in bare land.

In autumn period (Figure 13 (b)), the range of surface temperature is from 291.33 to 322.03 Kelvin with mean value of 302.02 Kelvin. Water and green vegetation still show lower land surface temperature while areas in bare land and some parts of built-up areas show higher temperatures.

Land surface temperature in winter is from 274.44 to 299.19 Kelvin with mean value of 283.59 Kelvin (Figure 13 (c)). Higher land surface temperatures appear in bare land and some built-up areas. Water, green vegetation and some built-up areas show lower temperatures.

During spring period, the land surface temperature is from 287.91 to 324.05 Kelvin with a mean of 301.29 Kelvin (Figure 13 (d)). The lower land surface temperatures appear in water and green vegetation while bare land and West of built-up areas show a higher land surface temperature distribution.

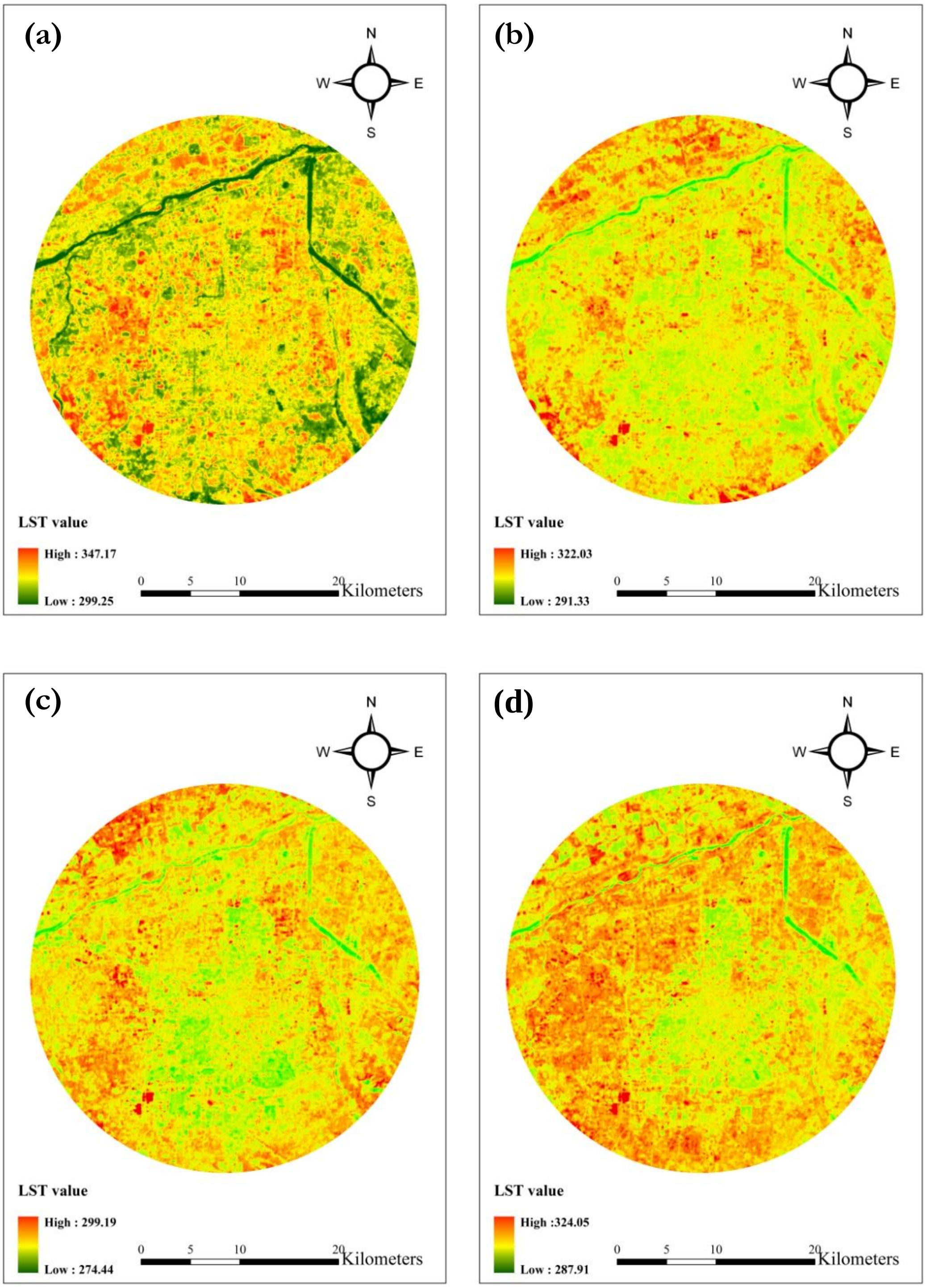

Figure 13：Land surface temperature maps (in Kelvin)：(a) summer; (b) autumn; (c) winter; (d) spring.

4.2.2. Quantification for the spatial patterns of land surface temperature in built-up areas

To analysis the spatial distribution of land surface temperature in built-up areas, the mean land surface temperature of built-up in each buffer zone for the four seasons are obtained based on the data of random sample points (shown in Table 17 to 20). Also the error bars for sample points in four seasons are showed in Figure 14 to 17.

Table 17: Mean and Std. Deviation of the land surface temperature of sample points in built-up areas in summer.

Summer	Number	Mean	Std. Deviation
buffer 1	30	316.03	1.69
buffer 2	80	317.05	2.41
buffer 3	80	317.39	2.58
buffer 4	80	316.62	2.57
buffer 5	75	316.46	2.11

Table 18: Mean and Std. Deviation of the land surface temperature of sample points in built-up areas in autumn.

Autumn	Number	Mean	Std. Deviation
buffer 1	30	301.89	1.50
buffer 2	80	302.14	1.67
buffer 3	100	303.06	2.03
buffer 4	95	302.54	2.11
buffer 5	85	302.61	1.74

Table 19: Mean and Std. Deviation of the land surface temperature of sample points in built-up areas in winter.

Winter	Number	Mean	Std. Deviation
buffer 1	30	283.17	1.50
buffer 2	77	282.50	1.46
buffer 3	100	283.76	2.18
buffer 4	75	283.43	1.81
buffer 5	60	283.18	1.38

Table 20: Mean and Std. Deviation of the land surface temperature of sample points in built-up areas in spring.

Spring	Number	Mean	Std. Deviation
buffer 1	30	300.13	2.14
buffer 2	80	300.87	2.57
buffer 3	115	302.06	2.48
buffer 4	80	301.75	2.63
buffer 5	50	301.44	2.22

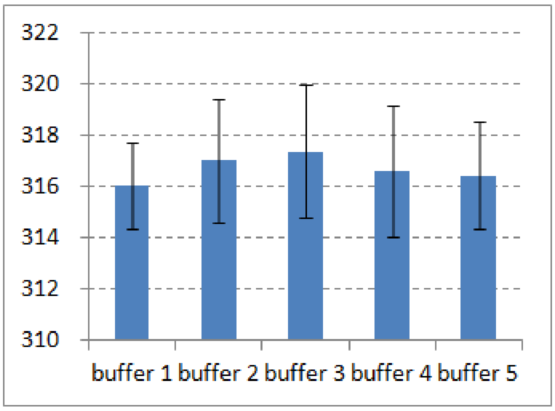

Figure 14: The error bar for the land surface temperature of sample points in built-up areas in summer

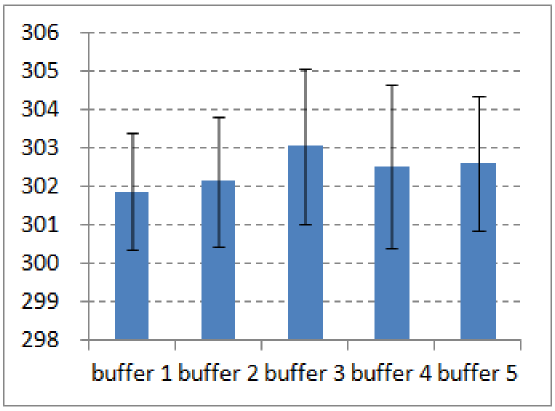

Figure 15: The error bar for the land surface temperature of sample points in built-up areas in autumn

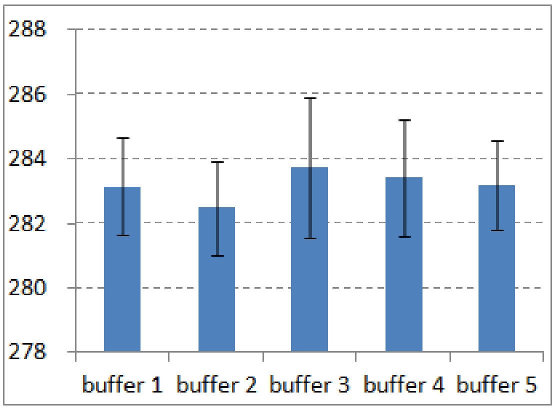

Figure 16: The error bar for the land surface temperature of sample points in built-up areas in winter

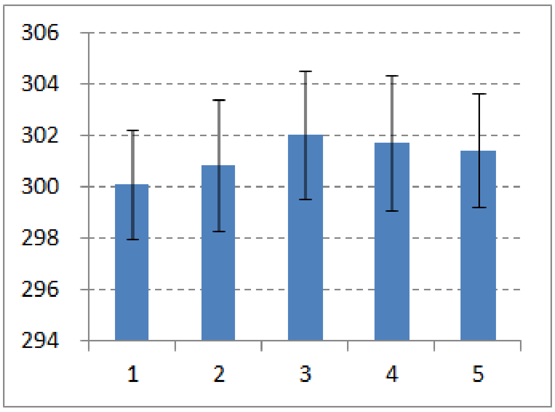

Figure 17: The error bar for the land surface temperature of sample points in built-up areas in spring

4.2.3. Quantification for the spatial patterns of urban heat island

In order to quantify the spatial patterns of urban heat island, randomly selecting sample points in each buffer zone is applied to obtain the information. Table 21 to 24 show the mean land surface temperature and standard deviation of sample points in each buffer zone, in the four seasons. In summer, the mean land surface temperature is highest in each buffer zone among the four seasons, while in winter, the mean land surface temperature is lowest. The mean land surface temperature in autumn is close to that in spring. Figure 18 to 21 are the error bar for the land surface temperature of sample points in the four seasons from the city centre to rural areas.

Table 21: Mean and Std. Deviation of the land surface temperature of sample points in each buffer in summer.

Summer	Number	Mean	Std. Deviation
buffer 1	30	315.68	2.36
buffer 2	90	316.60	2.33
buffer 3	150	316.70	3.62
buffer 4	210	315.79	3.72
buffer 5	270	315.75	3.88

Table 22: Mean and Std. Deviation of the land surface temperature of sample points in each buffer in autumn.

Autumn	Number	Mean	Std. Deviation
buffer 1	30	301.35	1.46
buffer 2	90	301.54	1.37
buffer 3	150	301.99	1.91
buffer 4	210	301.82	2.06
buffer 5	270	302.47	2.15

Table 23: Mean and Std. Deviation of the land surface temperature of sample points in each buffer in winter.

Winter	Number	Mean	Std. Deviation
buffer 1	30	283.08	1.58
buffer 2	90	283.22	1.08
buffer 3	150	283.46	1.64
buffer 4	210	283.51	1.60
buffer 5	270	284.04	1.60

Table 24: Mean and Std. Deviation of the land surface temperature of sample points in each buffer in spring.

Spring	Number	Mean	Std. Deviation
buffer 1	30	299.78	2.90
buffer 2	90	300.53	2.24
buffer 3	150	301.11	2.45
buffer 4	210	301.50	2.81
buffer 5	270	301.52	2.56

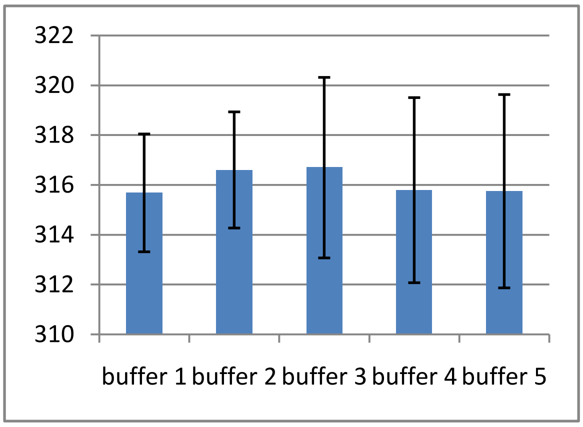

Figure 18: The error bar for the land surface temperature of sample points in each buffer in summer.

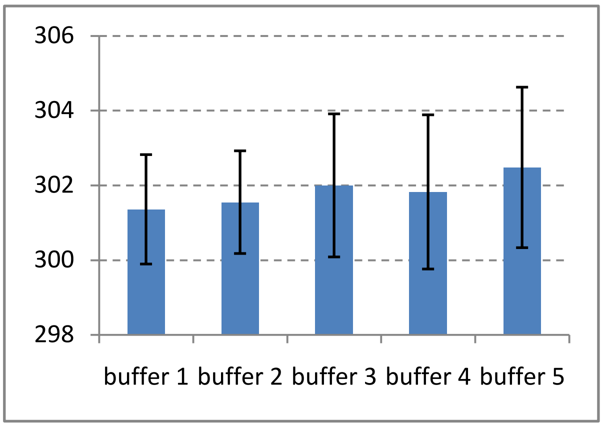

Figure 19: The error bar for the land surface temperature of sample points in each buffer in autumn.

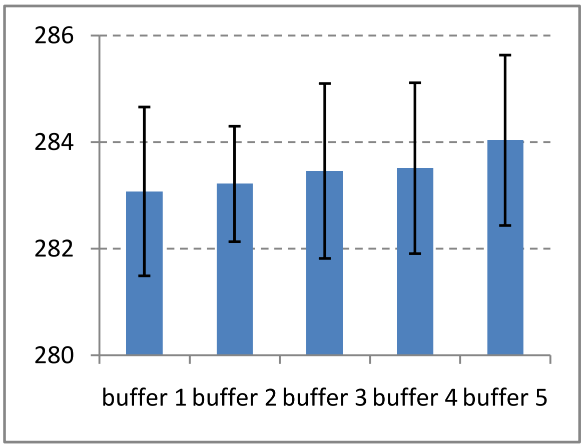

Figure 20: The error bar for the land surface temperature of sample points in each buffer in winter.

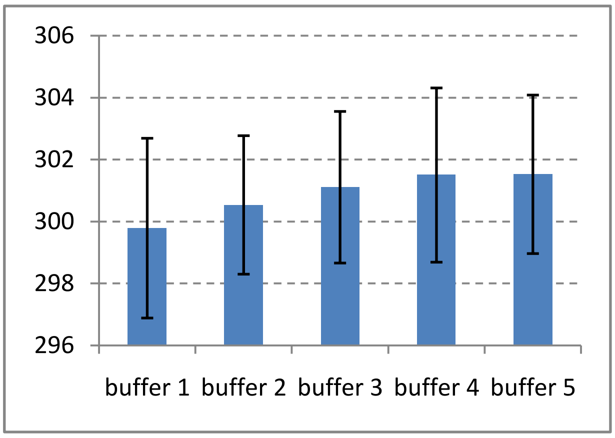

Figure 21: The error bar for the land surface temperature of sample points in each buffer in spring.

4.3. Relationship analysis between green-vegetated areas and urban heat island

4.3.1. Relationship between the green-vegetated areas and land surface temperature in built-up areas.

Firstly, the results of Z-test for proportion of green vegetation areas are showed in Table 25 - 28 with red mark representing the Z-Score is bigger than 1.96 or less than -1.96 and showing which two buffer zones have a statically significant difference between the proportion of vegetation areas.

In summer, the proportions of vegetation areas are significantly different between buffer 1 and 4, buffer 1 and 5, buffer 2 and 4, buffer 2 and 5, buffer 3 and 4, and buffer 3 and 5. In autumn, the difference of proportions between buffer 1and 2, buffer 1 and 2, buffer 3 and 4, and buffer 4 and 5, are not significant. During Winter and spring, the significant difference of proportions are both happens between buffer 1 and 5, buffer 3 and 5, and buffer 4 and 5, whereas there is also a significant difference between buffer 2 and 5 in winter.

Table 25: The result of Z-test for proportions, in summer.

Summer	buffer 1	buffer 2	buffer 3	buffer 4	buffer 5
buffer 1	----				
buffer 2	-0.19	----			
buffer 3	-1.30	-1.70	----		
buffer 4	-2.71	-4.02	-2.79	----	
buffer 5	-3.33	-5.07	-4.11	-1.36	----

Table 26: The result of Z-test for proportions, in autumn.

Autumn	buffer 1	buffer 2	buffer 3	buffer 4	buffer 5
buffer 1	----				
buffer 2	-0.14	----			
buffer 3	-1.55	-2.14	----		
buffer 4	-2.47	-3.63	-1.69	----	
buffer 5	-2.75	-4.14	-2.25	-0.53	----

Table 27: The result of Z-test for proportions, in winter.

Winter	buffer 1	buffer 2	buffer 3	buffer 4	buffer 5
buffer 1	----				
buffer 2	0.12.	----			
buffer 3	0.06	-0.10	----		
buffer 4	-0.70	-1.23	-1.37	----	
buffer 5	-2.14	-3.68	-4.49	-3.73	----

Table 28: The result of Z-test for proportions, in spring.

Spring	buffer 1	buffer 2	buffer 3	buffer 4	buffer 5
buffer 1	----				
buffer 2	-0.19	----			
buffer 3	-0.57	-0.59	----		
buffer 4	-1.38	-0.59	-1.66	----	
buffer 5	-3.13	-1.95	-5.54	-4.55	----

Secondly, the results of significant difference test for the land surface temperature in built-up areas in five buffer zones are showed in four box-plots shown in Figure 22.

In the (a) summer period, the land surface temperature of built-up in buffer 3 is significantly higher than that in buffer 1, 4 and 5 with the p value of 0.04, 0.011 and 0.015 respectively.

In autumn (b), the built-up land surface temperature of buffer 3 is significantly higher than that in buffer 1,2 and 4. Also, the significant differences exist between buffer 1 and 5 and between buffer 2 and 5 with the higher land surface temperature in buffer 5.

In winter (c), the land surface temperature of built-up in buffer 2 is statistically significant lower than that in buffer 4 and 5.

During spring period (d), the land surface temperature of built-up in buffer 1 is significantly lower than that in buffer 3, 4 and 5. Similarly, in buffer 2, the land surface temperature of built- up areas is also significantly lower than that in buffer 3 and 4.

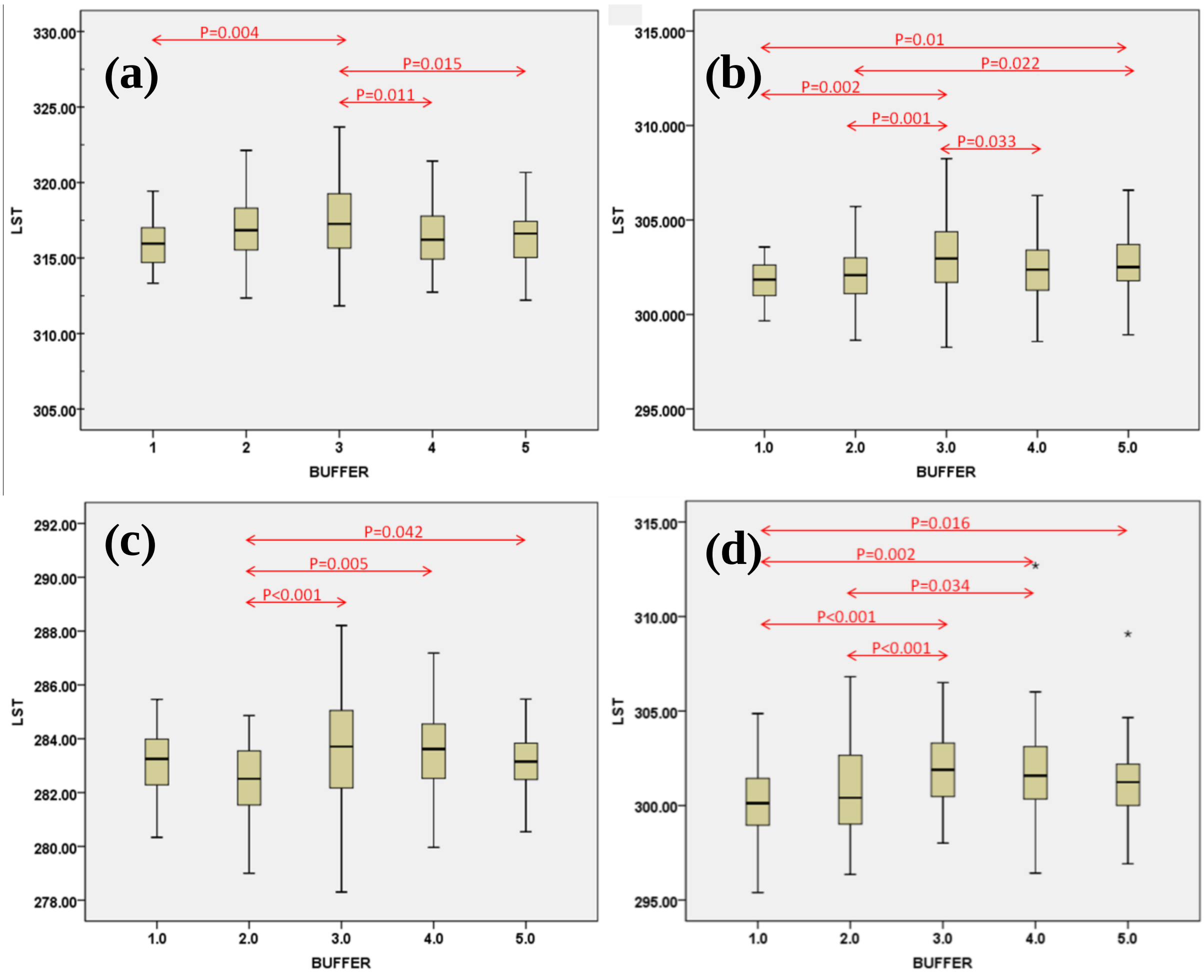

Figure 22: Four box-plots for the land surface temperature in built-up areas: (a) summer; (b) autumn; (c) winter; (d) spring.

Comparing the results of statistical results for the proportion of green vegetation areas and the land surface temperature in built-up areas between buffer zones, the relationships between green vegetation and land surface temperature of built-up exist between buffer 3 and buffer 4, also between buffer 4 and buffer 5 with negative correlation in summer. In autumn, positive relations happen between buffer 1 and 5, buffer 2 and 3, also between 2 and 5. In winter, the relationship exists between buffer 2 and buffer 5, as well as between buffer 1 and buffer 5 in spring.

4.3.2. Relationship between green-vegetated areas and urban heat island

In this section, the statistical results for quantified spatial patterns of urban heat island are present in Figure 23.

In autumn, based on the results shown in Figure 10 (b), the positive relationships between green vegetation and land surface temperature exist within buffer 2 and buffer 3, and also from buffer 4 to buffer 5, while a negative relation appears within buffer 3 and buffer 4.

In winter, related to Figure (c), the area proportion of green vegetation is similar in areas from buffer 1 to buffer 3, whereas in buffer 5, the area proportion increase. Therefore, there is a positive relationship existing from buffer 4 to buffer 5.

Accordingly, during spring , the area proportion of green vegetation raise gently from city centre to buffer 4, thus the vegetation is slightly positive related to land surface temperature from city centre to rural areas buffer 4.

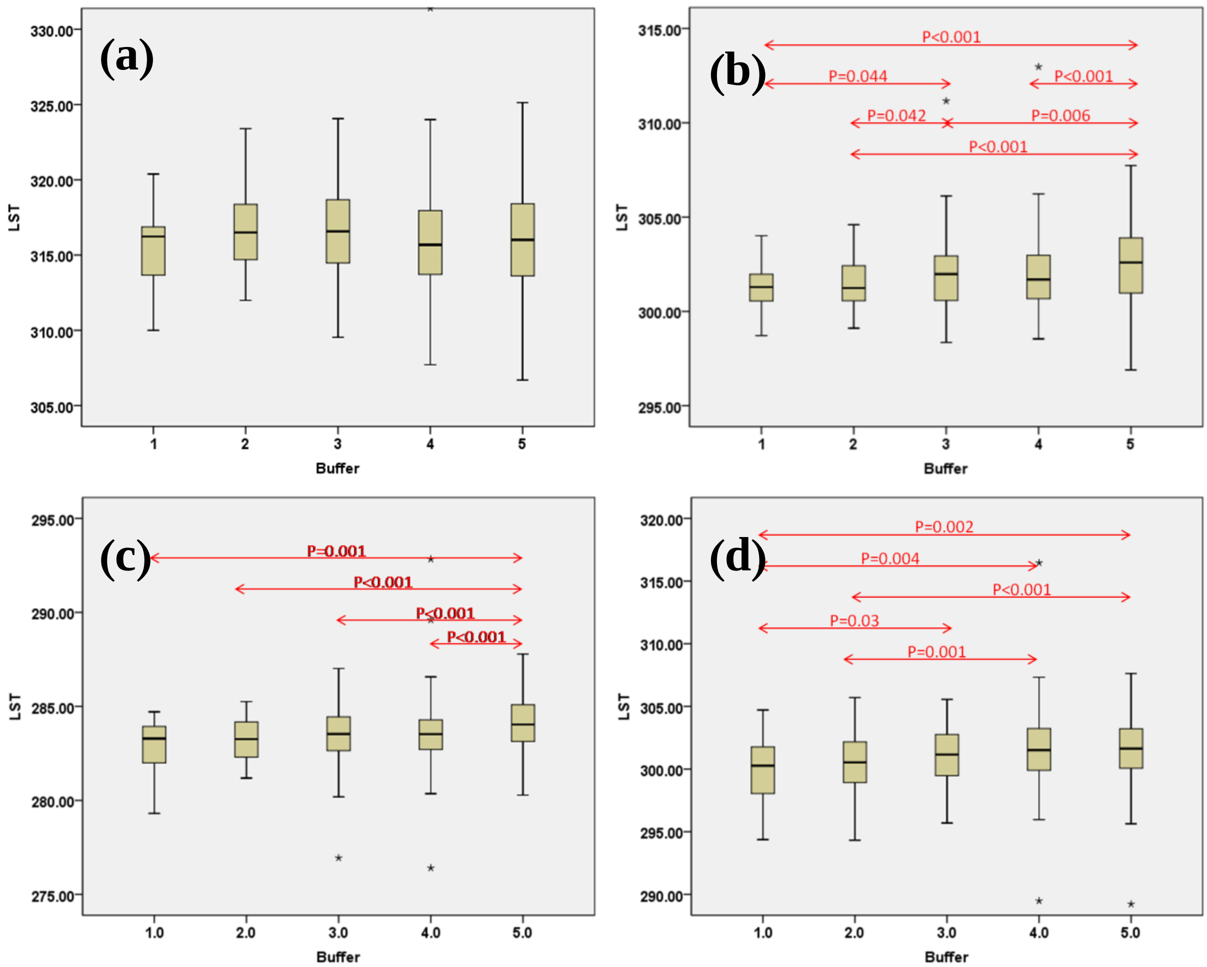

Figure 23: Four box-plots for the land surface temperature: (a) summer; (b) autumn; (c) winter; (d) spring.

Comparing the results of statistical results for the proportion of green vegetation areas and land surface temperature between buffer zones, there is no relationship happened in summer. In autumn, the relationships between green vegetation and urban heat island exist between buffer 1 and buffer 5, between buffer 2 and 3 as well as between buffer 2 and buffer 5. In winter, the relationship exists between buffer 1 and 5, buffer 2 and 5, buffer 3 and 5 as well as buffer 4 and 5. In spring, the correlation only happens between 1 and 5. These relationship are all positive.

5. DISCUSSIONS

5.1. Quantification for spatial patterns of green-vegetated areas in four seasons

Generally, the proportions of Green vegetation gradually increase from buffer 1 to buffer 5 in the four seasons. Especially in summer, the proportion of green vegetation is highest in the four seasons followed by the proportion in summer. In summer, the main crop is wheat. However, according to the agricultural phenology in Xi'an city, the wheat are harvested around the 15th June and then the land cover green vegetation turns into bare land. In autumn, some crops, for examples maize, are planted and begin to increase which brings out an increased proportion of green vegetation areas compared with summer. That's the reason why there are less green-vegetation areas in summer than in autumn. During winter period, the air temperature is lower and leaves fall, except for some winter crops in rural areas. Therefore, in this season, bare land occupies majority of the surrounding rural areas. As spring is coming, more healthy green vegetation appears around Xi'an city.

5.2. Quantification for the spatial patterns of land surface temperature in four seasons

From the results of the quantified spatial patterns of land surface temperature in the built-up areas for the four seasons in section 4.2.2., it is showed that in summer, autumn and winter, from city centre to buffer 3, the land surface temperatures gradually increase and then descend in buffer 4 and 5. This is because from city centre to a certain distance (buffer 3), the built-up is the dominant land cover with less green vegetation areas in urban areas, leading to a higher land surface temperature than rural areas.

From the results of the quantified spatial patterns of land surface temperature in each buffer zone for the four seasons in section 4.2.3., it is the similar increasing land surface temperature to that in built-up areas. High density of built-up contributes most in these buffers. With the further distance from city centre, the land cover contains more proportion of green vegetation and bare land areas while built- up areas decrease and getting more disperse. Therefore in buffer 4, the land surface temperature descends in summer and autumn. In buffer 5, the reason why the land surface temperature stays higher is that although the area of green vegetation increase, the area of bare land also goes up. According to literature, one research in the middle part of Jilin Province, China, found that the land surface temperature of bare land is higher than that of built-up areas (Guanglei et al., 2009). The same result is also found in the dynamism of land use changes on land surface temperature in Kenya(Mumina & Mundia, 2014). The reason why the higher temperature appears in bare land is that, in daytime, the bare land surface gets noticeably hotter as they absorb heat. Its high insolation, low heat capacity, and lack of evaporative cooling cause the higher land surface temperature in bare land (Mumina & Mundia, 2014). Besides, the colour of bare land is dark with the lower reflectivity and therefore, the ability of absorbing heat energy for bare land is higher than built-up surface materials and the temperature increases more quickly. During night, bare land releases heat and cool down. However, due to the high concentrated density in urban areas, it is more hard to carry on ventilation and abstracting heat, therefore the surface temperature of built-up areas is higher in night (Yan et al., 2011). In this research, the Landsat satellite passes the study area is around 11:00 am, which is coincident with the situation of daytime and the built-up surfaces have not reach the highest temperature in the day . Therefore, the land surface temperature of bare land is higher than that of other land cover types.

In the spatial patterns of land surface temperature in winter and spring, the land surface temperatures appear increasing trend from the city centre to rural areas. The reason is also about the endothermic character of bare land in daytime .

5.3. The relationship between green-vegetated areas and urban heat island

In the analysis of relation between green vegetation and land surface temperature in built-up areas, it is found that in summer, in rural areas, the vegetation has negative effect on the nearby built-up land surface temperature. This is because the proportion of green vegetation is higher in rural areas, which can contribute more to cool down the land surface temperature in far built-up areas. Beyond the higher density built-up areas, the land is more flat with a great stretch of green vegetation which can ameliorate the built-up microclimate through sunlight interception, shading and control of wind velocity, thereby decreasing the land surface temperature (Arc.N.I.OBI, 2014). Also, vegetation increases the moisture in the air, absorbs radiation from sun and cools the surrounding environment and thereby eliminate the urban heat island effects (Arc.N.I.OBI, 2014). Besides, the result is been concluded in the research for the impact of vegetation growth on the land surface temperature distribution in urban that there is strong negative relationship between land surface temperature of built-up areas and NDVI and also the green vegetation helps to reduce the land surface temperature in an area (Buyadi et al., 2014). It is also found that there is no relationship appears to describe the effects of green vegetation on land surface temperature in built-up areas. In urban areas, high density of built-up areas with poor ventilation may be a factor to influence the cooling effect of green vegetation, which may counteract a negative relation between vegetation and land surface temperature in built-up area.

In winter and spring, the positive relationship between green vegetation and land surface temperature occur in the comparison between rural areas and urban areas. Compared the proportion of green vegetation in urban areas, the proportion of vegetation is higher in rural areas. However, in these two seasons, the overall proportion of green-vegetated areas are lower compared with other that in summer and autumn. Besides, in these two seasons, bare land occupy the main land cover and it may influence the cooling effects of green-vegetation and result in a positive relationship between green vegetation and land surface temperature in built-up areas.

In the analysis of relationship between spatial patterns of green vegetation and land surface temperatures for all land cover types together, there is no relationship between green vegetation and urban heat island in summer. This is may be due to the wheat is harvest around 15th June, however, the summer Landsat 8 image used in this study is 25th June, which cannot show the real negative relationship between green vegetation and urban heat island in summer. In summer, winter and spring, there are positive relationship between green vegetation and urban heat island. This is maybe also the influence from the bare land with highest land surface temperature. In rural areas, the land cover mainly consists green vegetation and bare land winter and spring , thus influence the land surface temperature in rural areas.

In summary, in the analysis between green vegetation and land surface temperature in built-up areas, and the whole urban heat islands, it is found that the green vegetation has negative on cooling the surrounding temperature, however, the urban heat island not only is related to green vegetation, but also a combination results from the other land covers.

Besides, it is also found out that land surface temperature is sensitive to the moisture content in the atmosphere as well as vegetation cover (Mumina & Mundia, 2014). That is because more vegetation cover brings more evaporation in the air close to land surface which influence the moisture content. Therefore the evaporation cooling of vegetation is one efficient way of passive cooling for built-ups and urban spaces in hot regions (Robitu et al., 2006).

6. CONCLUSIONS AND RECOMMENDATIONS

6.1. General conclusion

This research has been undertaken to estimate land surface temperature and to investigate the relationship between spatial pattern of green vegetation in four seasons and urban heat islands through land surface temperature. This section gives a synthesis about the results of this study with the verification of hypotheses. The specific conclusions drawn from this study can be summarized as follows:

What are the seasonal distribution patterns of the green-vegetated areas in and around Xi'an City?

In all seasons the area of green vegetation increases with increasing distance from the city centre. Comparing the four seasons, in autumn, the area of green vegetation in each buffer zone is largest, followed by in summer, whereas in winter, the area is smallest. The areas of bare land is generally increasing from city centre to rural areas, especially in winter, the total area is largest of all four seasons, in all buffer zones.

What is the seasonal pattern of the land surface temperature in and around Xi'an City?

In summer, the land surface temperature is highest of all four seasons and in winter, the land surface temperature is lowest. The land surface temperature in autumn is nearly the same as in spring. Higher land surface temperature happens in bare land, followed by built-up and green vegetation and water occupy lower land surface temperatures. This is because in daytime, the colour of bare land is dark with the lower reflectivity, the ability of absorbing heat energy is higher than built-up surface materials and the temperature increases more quickly. Therefore, the land surface temperature of bare land is higher than that of other land cover types.

Does the seasonal patterns of green-vegetated areas in and around the city areas have a significant effect on urban heat island?

In summer, the effect of green vegetations on the land surface temperature in built-up areas is negative. In winter and spring, although the proportion of green vegetation is higher in rural areas than in urban areas, the overall proportion of green vegetation is relatively lower while the proportion of bare land is higher which may has influence on the spatial patterns of land surface temperature in built-up areas.

The relationship between the spatial patterns of green vegetation and land surface temperature is not clear in summer because the date of data used is after the harvest of crops. In other three season, the relationship is influenced by the large proportion of bare land with higher land surface temperatures.

6.2. Recommendations

(1) From this research, it is obtained that green vegetation has effects on minimizing urban heat islands and bare land is one factor to increase the total trend of land surface temperature in rural areas. Therefore, in future urban planning or urban construction in Xi'an city, it is better to replace bare land by green vegetation or evergreen trees to cooling down temperature and also plan more green spaces in urban areas to cool down the temperature and minimize the urban heat islands effect.

(2) In order to further researches on seasonal urban heat islands in Xi'an city, it is better to carry on field work to get more specific land cover types and more accurate spatial distribution of land surface temperature in four seasons. Besides, in this study, the satellite image in summer is on 25th June. In order to depict more typical summer land cover situation, choosing one clear satellite image dated before reaping wheat and getting more green vegetation in summer.

LIST OF REFERENCES

Ahmad, A., & Quegan, S. (2012). Analysis of Maximum Likelihood Classification on Multispectral Data. *Applied Mathematical Sciences*, *6*(129), 6425–6436.

Al-Fares, W. (2013). *Historical Land Use/Land Cover Classification Using Remote Sensing: A Case Study of the Euphrates River Basin in Syria* (p. 222). Springer Science & Business Media. Retrieved from https://books.google.com/books?id=2iGzGgPxzPQC&pgis=1

Arc.N.I.OBI. (2014). The Influence of Vegetation Microclimate in Hot Humid Tropical Environment-A case of Enugu Urban. *International Journal of Energy and Environmental Research*, *2*(2), 28–38.

Asmat, A., Mansor, S., & Hong, W. T. (2003). Rule Based Classification for Urban Heat Island Mapping Rule Based Classification for Urban Heat Island Mapping. *2nd FIG Regional Conference*, 1–11.

Borbora, J., & Das, A. K. (2014). Summertime Urban Heat Island study for Guwahati City, India. *Sustainable Cities and Society*, *11*, 61–66. doi:10.1016/j.scs.2013.12.001

Buyadi, S. N. A., Mohd, W. M. N. W., & Misni, A. (2013). Green Spaces Growth Impact on the Urban Microclimate. *Procedia - Social and Behavioral Sciences*, *105*, 547–557. doi:10.1016/j.sbspro.2013.11.058

Buyadi, S. N. A., Mohd, W. M. N. W., & Misni, A. (2014). Impact of vegetation growth on urban surface temperature distribution. *IOP Conference Series: Earth and Environmental Science*, *18*, 012104. doi:10.1088/1755-1315/18/1/012104

Canada. (2009). Climate Change and Health Adaptation Bulletin The Urban Heat Island Effect : Causes , Health Impacts and Mitigation Strategies. *Clean Air*, (1), 1–2. Retrieved from http://www.hc-sc.gc.ca/ewh-semt/alt_formats/hecs-sesc/pdf/pubs/climat/adapt_bulletin-adapt1/adapt_bulletin-adapt1-eng.pdf

Caselles, V., Rubio, E., Coll, C., & Valor, E. (1998). Thermal band selection for the PRISM instrument 3. Optimal Band Configurations. *Journal of Geophysical Research*, *103*(section 3), 57–67.

Congalton, R. G., & Green, K. (2002). *Assessing the Accuracy of Remotely Sensed Data: Principles and Practices* (p. 160). CRC Press. Retrieved from https://books.google.com/books?id=THm9VJ40-iQC&pgis=1

Courault, D., Courault, D., Seguin, B., Seguin, B., & Olioso, A. (2003). Review to estimate Evapotranspiration from remote sensing data: some examples from the simplified relationship to the use of mesoscale atmospheric models. *ICID Workshop on Remote Sensing of ET for Large Regions*, 1–18. doi:10.1007/s10795-005-5186-0

Farina, A. (2012). Exploring the relationship between land surface temperature and vegetation abundance for urban heat island mitigation in Seville , Spain, (15).

Foody, G. M. (2009). Classification accuracy comparison: Hypothesis tests and the use of confidence intervals in evaluations of difference, equivalence and non-inferiority. *Remote Sensing of Environment*, *113*(8), 1658–1663. doi:10.1016/j.rse.2009.03.014

Gago, E. J., Roldan, J., Pacheco-Torres, R., & Ordóñez, J. (2013). The city and urban heat islands: A review of strategies to mitigate adverse effects. *Renewable and Sustainable Energy Reviews*, *25*, 749–758. doi:10.1016/j.rser.2013.05.057

Guanglei, H., Hongyan, Z., Yeqiao, W., Zhihe, Q., & Zhengxiang, Z. (2009). Retrieval and Spatial Distribution of Land Surface Temperature in the Middle Part of Jilin Province Based on MODIS Data. *SCIENTIA GEOGRAPHICA SINICA*, *30*(3), 421–427.

Hadjimitsis, D. G., Papadavid, G., Agapiou, A., Themistocleous, K., Hadjimitsis, M. G., Retalis, A., … Clayton, C. R. I. (2010). Atmospheric correction for satellite remotely sensed data intended for agricultural applications: impact on vegetation indices. *Natural Hazards and Earth System Science*, *10*(1984), 89–95. doi:10.5194/nhess-10-89-2010

Howard, L. (1988). *The Climate of London* (Vol. 1, p. 285).

Imhoff, M. L., Zhang, P., Wolfe, R. E., & Bounoua, L. (2010). Remote sensing of the urban heat island effect across biomes in the continental USA. *Remote Sensing of Environment*, *114*(3), 504–513. doi:10.1016/j.rse.2009.10.008

IPCC. (2007). Climate Change 2007:Synthesis Report An Assessment of the Intergovernmental Panel on Climate Change, (November), 12–17.

Jia, X., & Richards, J. . (1994). Efficient maximum likelihood classification for imaging spectrometer data sets. *IEEE Transactions on Geoscience and Remote Sensing*, *32*(2), 274–281. doi:10.1109/36.295042

Jiménez-muñoz, J. C., Sobrino, J. A., Skokovi, D., Mattar, C., & Cristóbal, J. (2014). Land Surface Temperature Retrieval Methods From Landsat-8 Thermal Infrared Sensor Data, *11*(10), 1840–1843.

Li, X., Zhou, W., Ouyang, Z., Xu, W., & Zheng, H. (2012). Spatial pattern of greenspace affects land surface temperature: evidence from the heavily urbanized Beijing metropolitan area, China. *Landscape Ecology*, *27*(6), 887–898. doi:10.1007/s10980-012-9731-6

Liu, W., Ji, C., Zhong, J., Jiang, X., & Zheng, Z. (2006). Temporal characteristics of the Beijing urban heat island. *Theoretical and Applied Climatology*, *87*(1-4), 213–221. doi:10.1007/s00704-005-0192-6

Mahiny, A. S., & Turner, B. J. (2007). A comparison of four common atmospheric correction methods. *Photogrammetric Engineering & Remote Sensing*, *73*(4), 361–368. doi:10.14358/PERS.73.4.361

Maimaitiyiming, M., Ghulam, A., Tiyip, T., Pla, F., Latorre-Carmona, P., Halik, Ü., … Caetano, M. (2014). Effects of green space spatial pattern on land surface temperature: Implications for sustainable urban planning and climate change adaptation. *ISPRS Journal of Photogrammetry and Remote Sensing*, *89*, 59–66. doi:10.1016/j.isprsjprs.2013.12.010

McDonald, J. H. (2014). Handbook of Biological Statistics (3rd ed.). Retrieved February 17, 2015, from http://www.biostathandbook.com/kruskalwallis.html

Mumina, J. M., & Mundia, C. N. (2014). Dynamism of Land use Changes on Surface Temperature in Kenya : A Case Study of Nairobi City. *International Journal of Science and Research*, *3*(4), 38–41.

Qin, Z., Li, W., Gao, M., & Zhang, H. (2006). <title>Estimation of land surface emissivity for Landsat TM6 and its application to Lingxian Region in north China</title>, *6366*, 636618–636618–8. doi:10.1117/12.689310

R, R., & D.Schlapfer. (2014). Atmospheric / Topographic Correction for Satellite Imagery (ATCOR - 2/3 User Guide). *ATCOR-2/3 User Guide, Version 8.3.1*, (February).

Rajeshwari, A., & Mani, N. D. (2014). Estimation of Land Surface Temperature of Dindigul District Using Landsat 8 Data. *International Journal of Research in Engineering and Technology*, *03*(05), 122–126.

Robitu, M., Musy, M., Inard, C., & Groleau, D. (2006). Modeling the influence of vegetation and water pond on urban microclimate. *Solar Energy*, *80*, 435–447. doi:10.1016/j.solener.2005.06.015

Rozenstein, O., Qin, Z., Derimian, Y., & Karnieli, A. (2014). Derivation of land surface temperature for Landsat-8 TIRS using a split window algorithm. *Sensors (Basel, Switzerland)*, *14*(4), 5768–80. doi:10.3390/s140405768

Rutherford, A. (2001). *Introducing Anova and Ancova: A GLM Approach* (p. 182). SAGE Publications. Retrieved from https://books.google.com/books?id=T6uvhsy8d_8C&pgis=1

Schwarz, N., Schlink, U., Franck, U., & Großmann, K. (2012). Relationship of land surface and air temperatures and its implications for quantifying urban heat island indicators—An application for the city of Leipzig (Germany). *Ecological Indicators*, *18*, 693–704. doi:10.1016/j.ecolind.2012.01.001

Srivastava, P. K., Han, D., Rico-Ramirez, M. a., Bray, M., & Islam, T. (2012). Selection of classification techniques for land use/land cover change investigation. *Advances in Space Research*, *50*(9), 1250–1265. doi:10.1016/j.asr.2012.06.032

Tao, M., Chen, L., Su, L., & Tao, J. (2012). Satellite observation of regional haze pollution over the North China Plain. *Journal of Geophysical Research: Atmospheres*, *117*(June), 1–16. doi:10.1029/2012JD017915

Timothy W. Hawkins, Anthony J. Brazel, William L. Stefanov, Wendy Bigler, E. M. S. (2004). The Role of Rural Variability in Urban Heat Island Determination for Phoenix , Arizona. *Tournal of Applied Meteorology*, *43*, 476–486.

Tursilowati, L., Tetuko, J., Sumantyo, S., Kuze, H., & Adiningsih, E. S. (2012). Relationship between Urban Heat Island Phenomenon and Land Use / Land Cover Changes in Jakarta – Indonesia Corresponding Author : Laras Tursilowati, *3*(4), 645–653.

UNFPA. (2008). The state of the world population 2007: Unleashing the potential of urban growth. Retrieved from http://www.ncbi.nlm.nih.gov/pubmed/18599934

Wan, Z., Dozier, J., & Member, A. (1996). A Generalized Split- Window Algorithm for Retrieving Land-Surface Temperature from Space, *34*(4), 892–905.

Weng, Q., Lu, D., & Schubring, J. (2004). Estimation of land surface temperature–vegetation abundance relationship for urban heat island studies. *Remote Sensing of Environment*, *89*(4), 467–483. doi:10.1016/j.rse.2003.11.005

Yan, D., Xingming, L., Yanchao, Y., Fanqiang, W., & Chuanli, D. (2011). Distributive characters of urban heat island effect in Xi'an City. *Journal of Arid Land Resources and Environment*, *25*(8), 107–112.

Yu, Y., Privette, J. L., & Pinheiro, A. C. (2008). Evaluation of Split-Window Land Surface Temperature Algorithms for Generating Climate Data Records. *IEEE Transactions on Geoscience and Remote Sensing*, *46*(1), 179–192. doi:10.1109/TGRS.2007.909097

Yuan, F., & Bauer, M. E. (2007). Comparison of impervious surface area and normalized difference vegetation index as indicators of surface urban heat island effects in Landsat imagery. *Remote Sensing of Environment*, *106*(3), 375–386. doi:10.1016/j.rse.2006.09.003

Zhang, B., Xie, G., Gao, J., & Yang, Y. (2014). The cooling effect of urban green spaces as a contribution to energy-saving and emission-reduction: A case study in Beijing, China. *Building and Environment*, *76*, 37–43. doi:10.1016/j.buildenv.2014.03.003

Zhang, X. X., Wu, P. F., & Chen, B. (2010). Relationship between vegetation greenness and urban heat island effect in Beijing City of China. *Procedia Environmental Sciences*, *2*, 1438–1450. doi:10.1016/j.proenv.2010.10.157

Zhao, S., Qin, Q., Yang, Y., Xiong, Y., & Qiu, G. (2005). Comparison of two split-window methods for retrieving land surface temperature from MODIS data. *I.Earth Syst. Sci*, *118*(4), 345–353.

APPENDIX 1

In the Split-Window (SW) algorithm, one kind of parameters is brightness temperature for band 10 and band 11. Figure 16, 17, 18 and 19 show the Brightness temperature maps for two bands 10 and 11 in four images.

The brightness temperatures within two bands are not the same, and among four seasons are different. For the bands 10 and 11, because of the difference between reflectance rescaling coefficients, thermal constants and absorbed wavelength, derived results differ kindly and the value for band 10 is a litter bit higher than band 11. Among the brightness temperature of band 10 four seasons, the mean value are 311.268, 297.691, 278.923 and 293.957 (Kelvin) corresponding to summer, autumn, winter and spring respectively. These results is parallel to the natural phenomenon that spring is hot and winter is cold.

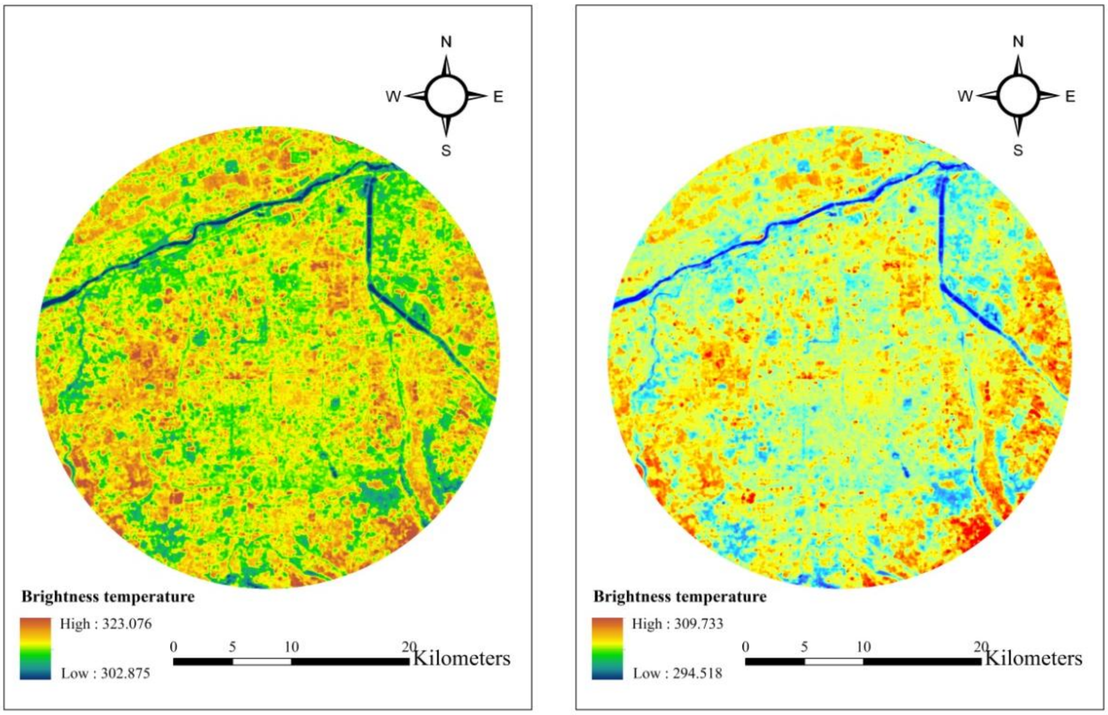

Figure 24: Brightness temperature maps for bands 10 (left) and 11 (right) in the image of summer (in Kelvin).

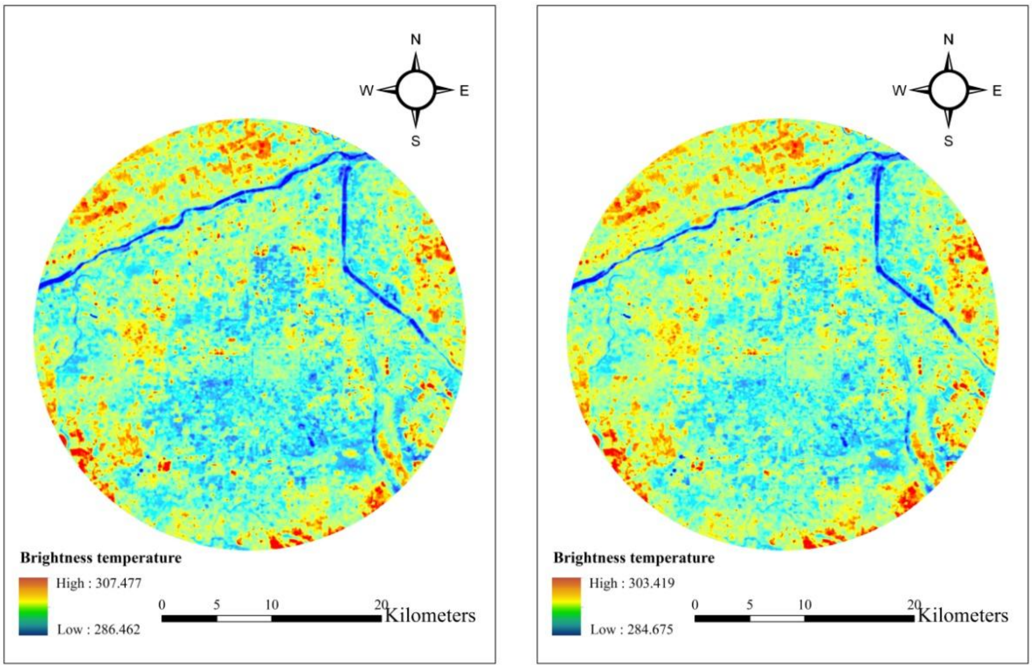

Figure 25: Brightness temperature maps for bands 10 (left) and 11 (right) in the image of autumn (in Kelvin).

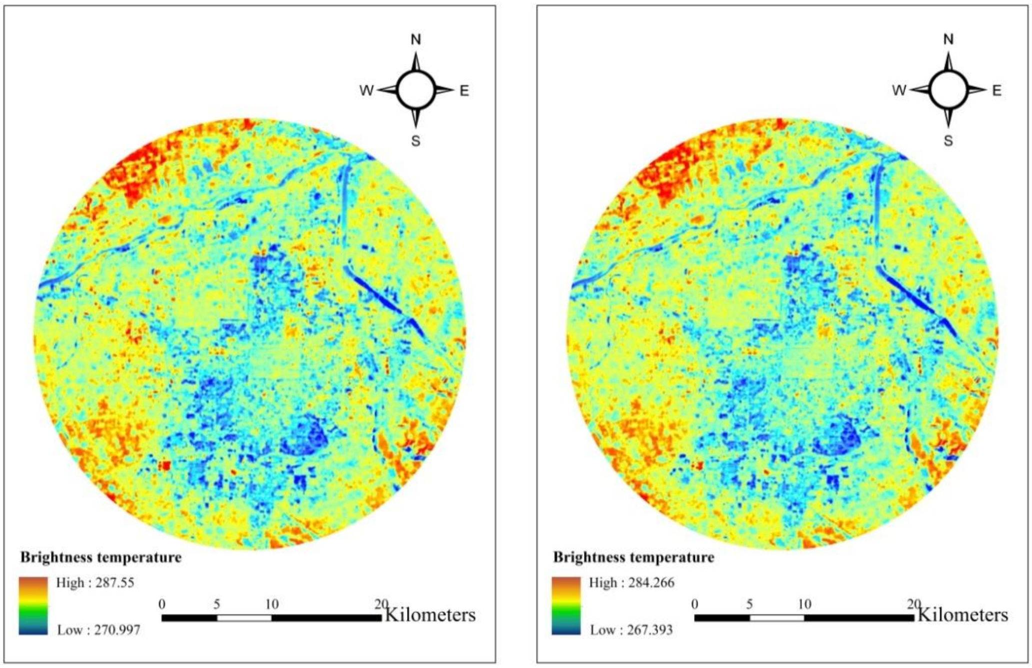

Figure 26: Brightness temperature maps for bands 10 (left) and 11 (right) in the image of winter (in Kelvin)

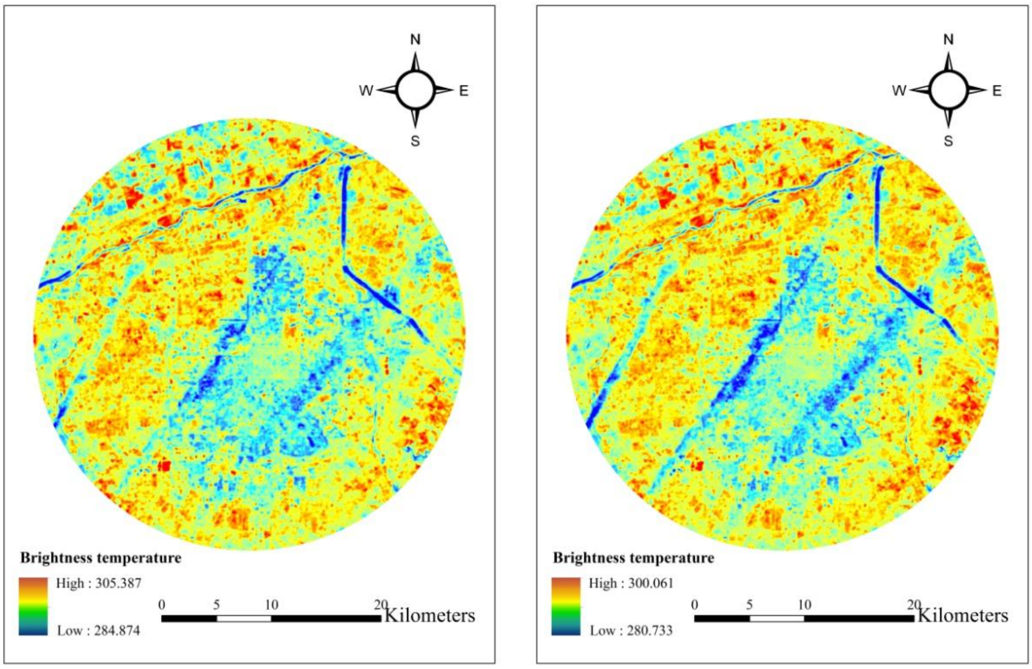

Figure 27: Brightness temperature maps for bands 10 (left) and 11 (right) in the image of spring (in Kelvin).

APPENDIX 2

One another input of Split-Window (SW) algorithm is land surface emissivity. The calculation of land surface emissivity is very important and due to the complicated heterogeneity in study area, the estimation of land surface emissivity is necessary to perform at pixel scale. Figure 20 shows the land surface emissivity of band 10 for four images.

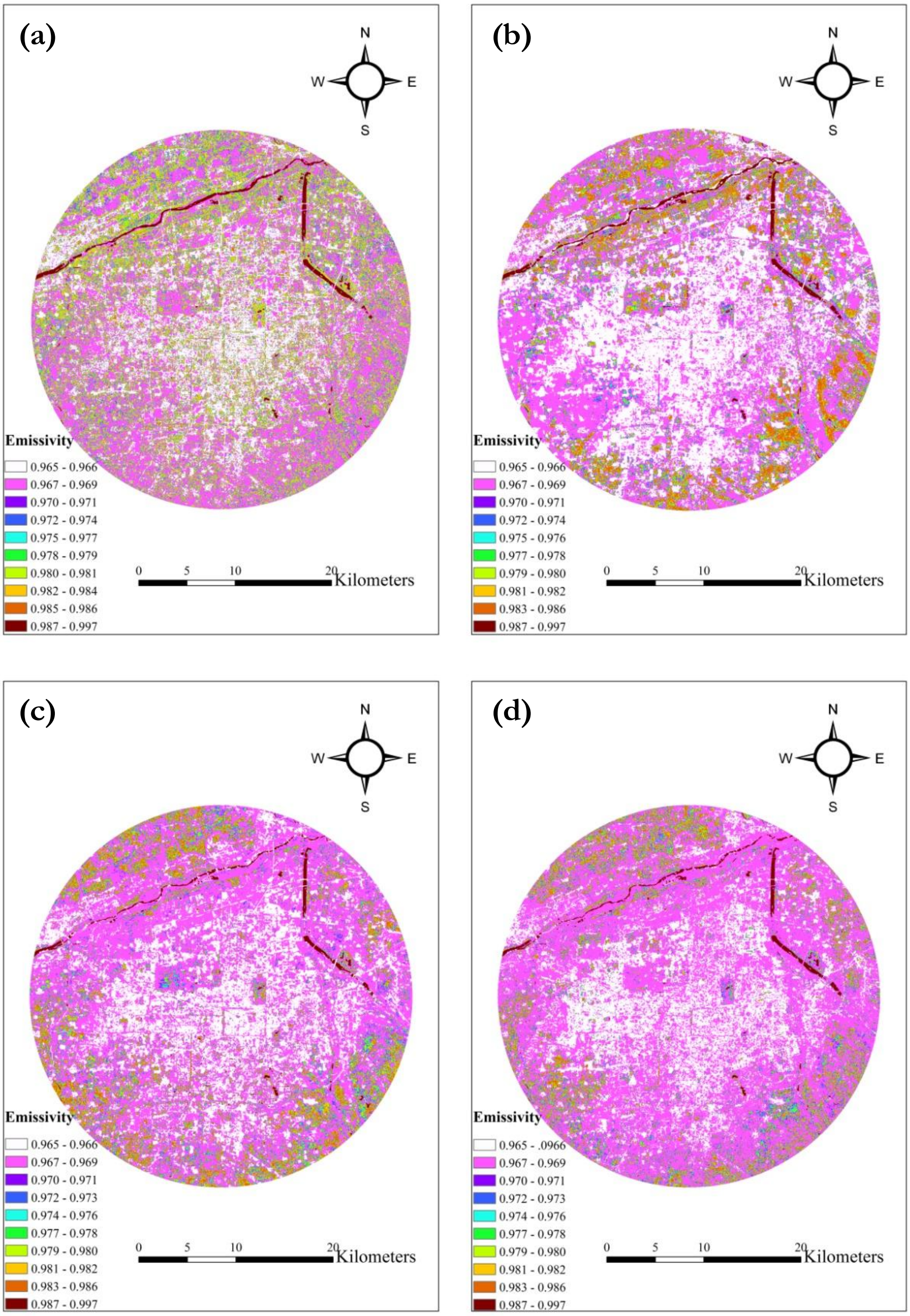

Figure 28: Land surface emissivity of band 10 for four images: (a) summer; (b) autumn; (c) winter; (d) spring.

Firstly, differences among these four images appear owing to NDVI value, fractional vegetation cover and land cover classification results. Seasonally, the NDVI value changes very widely which influence the fractional vegetation cover simultaneously. These results also imply the relationship between green vegetation and the distribution of land surface emissivity and land surface temperature.

Secondly, there are a few differences between the land surface emissivity of band 10 and band 11 and these differences are no more than 0.01. The cause of the dissimilarity is the emissivity (εi) of each land cover type for these two bands (showed in Table 9). Just because the distinguishes of two values, it minimize the error to estimate land surface temperature and make the result more accurate.

In addition to the overall difference among four images, there are also differences among land cover types. Table 18 presents the land surface emissivity values for each land cover.

Table 29: Land surface emissivity of bands 10 and 11 for each land cover type.

Image	Land cover type	NDVI value	Land surface emissivity (band 10)	Land surface emissivity (band 11)
June 25, 2013 (Summer)	Water	-0.197	0.997	0.993
	Built-up	0.204	0.969	0.978
	Vegetation	0.577	0.976	0.983
	Others	0.185	0.970	0.979
September 29, 2013 (Autumn)	Water	-0.085	0.997	0.993
	Built-up	0.086	0.966	0.976
	Vegetation	0.275	0.973	0.982
	Others	0.126	0.967	0.977
January 3, 2014 (Winter)	Water	-0.202	0.997	0.993
	Built-up	0.042	0.965	0.975
	Vegetation	0.315	0.978	0.985
	Others	0.130	0.969	0.979
March 24, 2014 (Spring)	Water	-0.159	0.997	0.993
	Built-up	0.076	0.965	0.975
	Vegetation	0.323	0.975	0.982
	Others	0.110	0.968	0.978